

NASA/CR—2005-213815



On Extending the Capabilities of COMPARE to Include Material Damage

Atef F. Saleeb and Thomas E. Wilt
University of Akron, Akron, Ohio

The NASA STI Program Office . . . in Profile

Since its founding, NASA has been dedicated to the advancement of aeronautics and space science. The NASA Scientific and Technical Information (STI) Program Office plays a key part in helping NASA maintain this important role.

The NASA STI Program Office is operated by Langley Research Center, the Lead Center for NASA's scientific and technical information. The NASA STI Program Office provides access to the NASA STI Database, the largest collection of aeronautical and space science STI in the world. The Program Office is also NASA's institutional mechanism for disseminating the results of its research and development activities. These results are published by NASA in the NASA STI Report Series, which includes the following report types:

- **TECHNICAL PUBLICATION.** Reports of completed research or a major significant phase of research that present the results of NASA programs and include extensive data or theoretical analysis. Includes compilations of significant scientific and technical data and information deemed to be of continuing reference value. NASA's counterpart of peer-reviewed formal professional papers but has less stringent limitations on manuscript length and extent of graphic presentations.
- **TECHNICAL MEMORANDUM.** Scientific and technical findings that are preliminary or of specialized interest, e.g., quick release reports, working papers, and bibliographies that contain minimal annotation. Does not contain extensive analysis.
- **CONTRACTOR REPORT.** Scientific and technical findings by NASA-sponsored contractors and grantees.

- **CONFERENCE PUBLICATION.** Collected papers from scientific and technical conferences, symposia, seminars, or other meetings sponsored or cosponsored by NASA.
- **SPECIAL PUBLICATION.** Scientific, technical, or historical information from NASA programs, projects, and missions, often concerned with subjects having substantial public interest.
- **TECHNICAL TRANSLATION.** English-language translations of foreign scientific and technical material pertinent to NASA's mission.

Specialized services that complement the STI Program Office's diverse offerings include creating custom thesauri, building customized databases, organizing and publishing research results . . . even providing videos.

For more information about the NASA STI Program Office, see the following:

- Access the NASA STI Program Home Page at <http://www.sti.nasa.gov>
- E-mail your question via the Internet to help@sti.nasa.gov
- Fax your question to the NASA Access Help Desk at 301-621-0134
- Telephone the NASA Access Help Desk at 301-621-0390
- Write to:
NASA Access Help Desk
NASA Center for AeroSpace Information
7121 Standard Drive
Hanover, MD 21076

NASA/CR—2005-213815



On Extending the Capabilities of COMPARE to Include Material Damage

Atef F. Saleeb and Thomas E. Wilt
University of Akron, Akron, Ohio

Prepared under Cooperative Agreement NCC3-992

National Aeronautics and
Space Administration

Glenn Research Center

September 2005

Available from

NASA Center for Aerospace Information
7121 Standard Drive
Hanover, MD 21076

National Technical Information Service
5285 Port Royal Road
Springfield, VA 22100

Available electronically at <http://gltrs.grc.nasa.gov>

Extending the Capabilities of COMPARE to Include Material Damage

Atef F. Saleeb and Thomas E. Wilt
The University of Akron
Akron, Ohio 44325-3905

1.0 Introduction

It is widely accepted that large-scale numerical simulations, based on the finite element method, provide a viable approach for assessing the integrity, reliability, and life expectancy of structural components operating under complex thermomechanical/multi-axial loading conditions. The practicality and predictive utility of this analysis depends heavily on three main factors: (i) the choice of suitable mathematical models which provide the macroscopic/phenomenological representations of the inelastic constitutive properties and materials damage; (ii) the associated algorithmic developments of efficient and robust schemes for their computer implementation; and (iii) the necessary characterization of the new damage material parameters. Because of their importance, each of these individual subjects has attracted considerable interest over the years. The present research work is concerned with these three areas, with particular emphasis on the material damage modeling; i.e., including both viscoelastic stiffness degradation and plastic strength reduction.

With regard to mathematical modeling in item (i) above, materials of interest here include variety of metallic superalloys and advanced multiphased (e.g., metal matrix) composites utilized in advanced engine and propulsion systems. Depending on the range of temperatures and loading rates under service conditions, these materials exhibit a multitude of complex phenomena, spanning the entire spectrum of ductile-transitional-brittle response modes. For example, this includes significant (time-dependent) inelastic deformations, coupled with progressive development of material damage due to distributed microdefects (e.g., microvoids and microcracking on the micro/meso scales), which later coalesces into distinct fracture modes at the end of the failure process (e.g., propagating macrocracks, or softening/localization zones).

On the computational side, the finite-element failure analyses for the given problem may be carried out with different levels of sophistication; e.g., from the simplest uncoupled approach to the fully coupled approach for progressive local damage to fracture initiation. These approaches, with their varying degrees of interactions, require specially designed segments of the analysis program, that is, their associated algorithmic “blocks” for the various damage mechanisms are necessary. Firstly, a common problem in all nonlinear analyses concerns the integration of the rate evolutionary equations in the underlying material constitutive models. At each iteration (step) of the incremental solution, these calculations are performed locally, on the material/integration-point level. To this end, the present work has utilized previously developed implicit time integration methods (refs. 1 to 3) because of their better stability, robustness, as well as wider range of applicability, compared to the earlier explicit counterparts.

The main objective of the present research has focused on devising computationally efficient methodologies for life predictions of structural components. To this end, the work involves several contributions in two broad areas; i.e., (i) mathematical modeling and (ii) algorithmic developments and (iii) characterization of material parameters. In the following sections we briefly describe some of the issues pertinent to the requirements mentioned above.

2.0 Extension of GVIPS with Stiffness and Strength Damage

As a basis for the mathematical modeling, theories of viscoplasticity, continuum-damage mechanics, and nonlinear fracture mechanics are typically utilized. In particular, the state-of-art in viscoplastic deformation modeling is currently very well developed in the form of the so-called internal variable formalism in thermodynamics for irreversible processes. The present work builds upon the recent class of potential-based models, in particular, the Generalized Viscoplasticity with Potential Structure, GVIPS, model developed in association with NASA Glenn. Here, damage is included to account for the softening due to stiffness and/or strength reduction mechanisms present in the material. For background material on the details of the inelastic deformation model, together with its associated computer-implementation algorithms, as well as automated characterization procedure, we refer to some of our previous publications; e.g., see (refs. 1 to 4). In the following, we will only give the details pertinent to the “new” extensions to include damage modes in the overall coupled-deformation models.

2.1 Mathematical Formulation

In this section we will outline the modifications to the GVIPS model to now allow for the modeling of both stiffness and strength damage. As with all of the model developments for the GVIPS class of models, the new additions are added in a “modular” fashion so as to build upon previous derivations and numerical coding. This approach is especially important for code maintenance issues in that previously implemented code may be “re-used” with a certain degree of certainty that it has been well tested and is stable. Figure 1 show’s exactly how the addition of the new damage capabilities was added to the existing overall implicit integration algorithm of the GVIPS model. Note how the new additions are treated as modules that are inserted in the appropriate location.

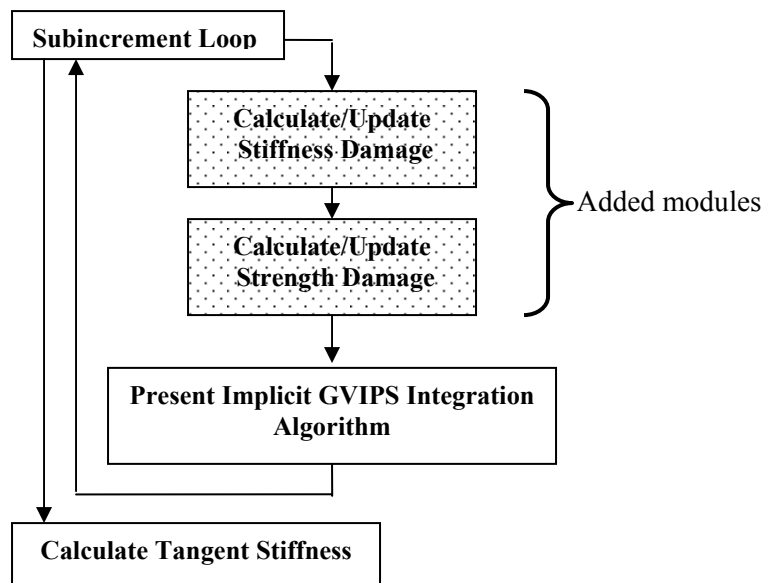


Figure 1.—Implicit Integration Scheme

2.1.1 Viscoelastic Material Stiffness Degradation.—Here we present the formulation for the stiffness damage component. The overall scheme of the stiffness damage is shown in the pseudo flowchart in figure 2. It is important to note that the evolution of damage is directly evaluated and does not require any iterative updates in the implicit integration scheme for the other stress and internal variables. The quantity Ψ is the measure of the amount of stiffness damage and varies from 1 to ∞ (1 being the virgin undamaged state). The parameter $\bar{\epsilon}$ is the current magnitude of the total strain and $\bar{\epsilon}_{cut}$ is referred to as the “cut-off” value, below which no damage is said to occur. In the present model, a single stiffness damage mechanism is utilized with a total of four parameters, $c_e, \bar{Y}_0, \mu_e, n_e$ introduced for characterizing the stiffness damage.

2.1.2 Viscoplastic Material Strength Reduction.—Similar to above, the overall scheme of the stiffness damage is shown in the pseudo flowchart in figure 3. Again note that the evolution damage is directly evaluated and does not require any iterative updates in the implicit integration scheme for the stress and internal variables. The quantity $\theta^{(b)}$ is the measure of the amount of strength reduction damage, for each mechanism (b), and varies from 1 to ∞ (1 being the virgin undamaged state). The parameter $\bar{\epsilon}^i$ is the current magnitude of the total inelastic strain and $\bar{\epsilon}_{cut}^i$ is referred to as the “cut-off” value, below which no strength damage is said to occur. A total of four parameters, $c_d^{(i)}, Y_0^{(i)}, \mu_d^{(i)}, n_d^{(i)}$ are introduced for the strength damage. For the case of strength damage, these four additional parameters are present for each viscoplastic mechanism.

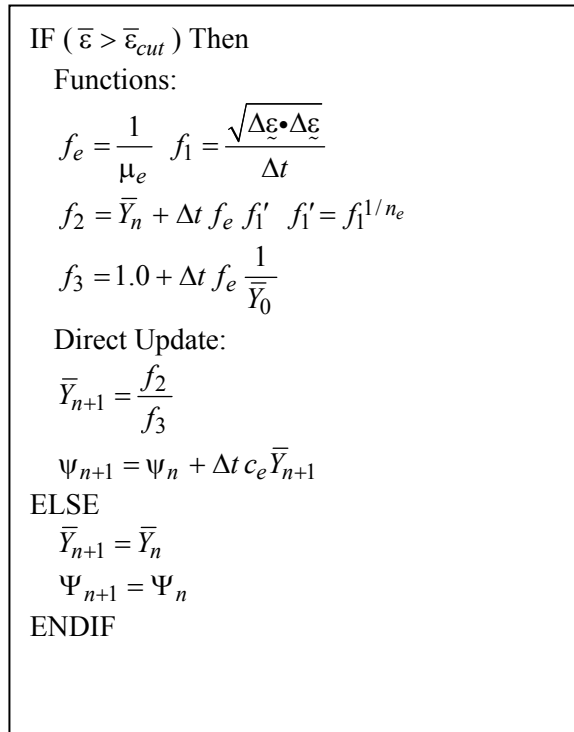


Figure 2.—Stiffness damage module.

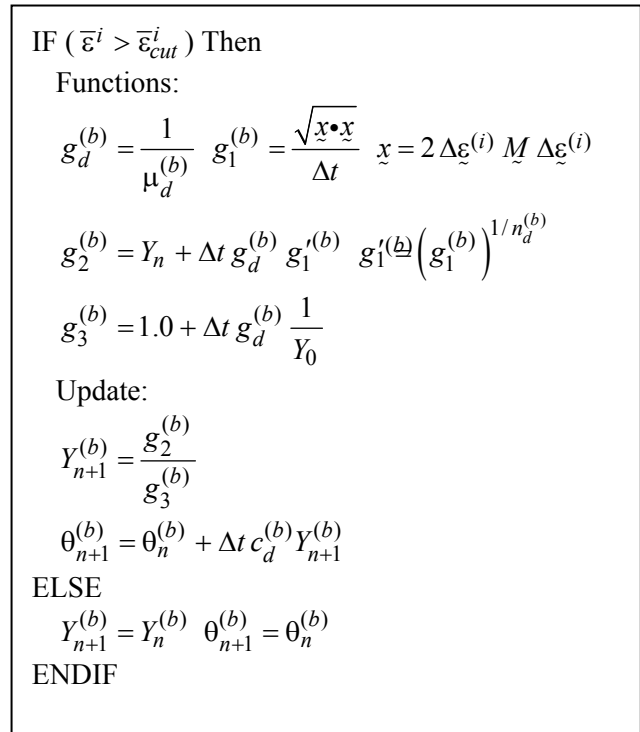


Figure 3.—Strength damage module.

2.2 Modifications to Implicit Routine

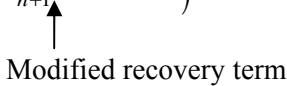
In this section, we present the necessary modifications to the previously developed implicit integration algorithm used for the GVIPS model. As with any implicit scheme, the residuals of the iterative quantities drive the iterations/corrections. Thus the stress and internal stress residuals were modified and are given below.

Stress Residual:

$$\mathbf{R}_\sigma = \boldsymbol{\sigma}_{n+1} - \left[\boldsymbol{\sigma}_n + \sum_{a=1}^{Nel} \left(e^{-\Delta t / \rho^a} - 1 \right) \mathbf{q}_{n+1}^a + \mathbf{C}^e \left(\Delta \boldsymbol{\varepsilon} - \Delta t f \boldsymbol{\Gamma} \right) - \underbrace{\Delta t (\psi_{n+1} - 1) \boldsymbol{\sigma}_{n+1}}_{\text{Additional term}} \right]$$

Internal Stress Residual:

$$\mathbf{R}_\alpha^{(b)} = \mathbf{Q}^{(b)} \left(\boldsymbol{\alpha}_{n+1}^{(b)} - \boldsymbol{\alpha}_n^{(b)} \right) - \Delta t \left(h^{(b)} f \boldsymbol{\Gamma}_{n+1}^{(b)} - \bar{r}^{(b)} \boldsymbol{\pi}^{(b)} \right) \quad \bar{r}^{(b)} = r^{(b)} + (\theta^{(b)} - 1)$$



Modified recovery term

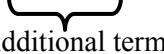
with the following quantities defined below,

$$\mathbf{Q}^{(b)} = \left[\mathbf{M} - \frac{h'(G^{(b)})}{h(G^{(b)})} \boldsymbol{\pi}^{(b)} \otimes \boldsymbol{\pi}^{(b)} \right] \quad f = \frac{F^n}{2\mu} \quad h^{(b)} = H^{(b)} \left[1 - \left(\frac{G^{(b)}}{\kappa_\alpha^{(b)}} \right)^{\beta^{(b)}} \right] \quad r^{(b)} = R^{(b)} \left(G^{(b)} \right)^{m^{(b)}}$$

$$F = \frac{1}{2\kappa_f^2} (\boldsymbol{\sigma} - \boldsymbol{\alpha}) : \mathbf{M} : (\boldsymbol{\sigma} - \boldsymbol{\alpha}) \quad G^{(b)} = \frac{1}{2(\kappa_\alpha^{(b)})^2} \boldsymbol{\alpha}^{(b)} : \mathbf{M} : \boldsymbol{\alpha}^{(b)} \quad \boldsymbol{\Gamma} = \mathbf{M} (\boldsymbol{\sigma} - \boldsymbol{\alpha}) \quad \boldsymbol{\pi}^{(b)} = \mathbf{M} \boldsymbol{\alpha}^{(b)}$$

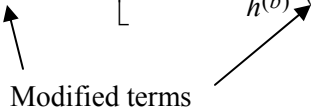
Another key component in the iterative process is the stiffness terms.

$$\mathbf{P}_3 = \left[1.0 + \Delta t (\psi - 1) \right] \mathbf{C}^{evp^{-1}} + \mathbf{P}_4 \quad \mathbf{P}_4 = \Delta t [f \mathbf{M} + f' \boldsymbol{\Gamma} \otimes \boldsymbol{\Gamma}] \quad \mathbf{P}_2 = h^{(b)} \mathbf{P}_4$$



Additional term

$$\mathbf{P}_1^{(b)} = \mathbf{Z}_m + \mathbf{P}_2^{(b)} + \Delta t \bar{r}^{(b)} \mathbf{M} + \left[\Delta t r'^{(b)} - \frac{h'(b)}{h(b)} (\Delta t \bar{\Gamma}^{(b)} + 1) \right] \boldsymbol{\pi}^{(b)} \otimes \boldsymbol{\pi}^{(b)}$$



Modified terms

In the above, the terms h' and r' signify derivatives, i.e.,

$$h'^{(b)} = \frac{1}{(\kappa_\alpha^{(b)})^2} \frac{\partial h(\cdot)}{\partial G^{(b)}} \quad r'^{(b)} = \frac{1}{(\kappa_\alpha^{(b)})^2} \frac{\partial r^{(b)}}{\partial G^{(b)}}$$

As one can see from the above equations, the modifications required in the existing implicit scheme were minimal. For further details of the implicit algorithm and the necessary equations, please refer to the paper by Saleeb et al (ref. 4) for further definitions of the above terms.

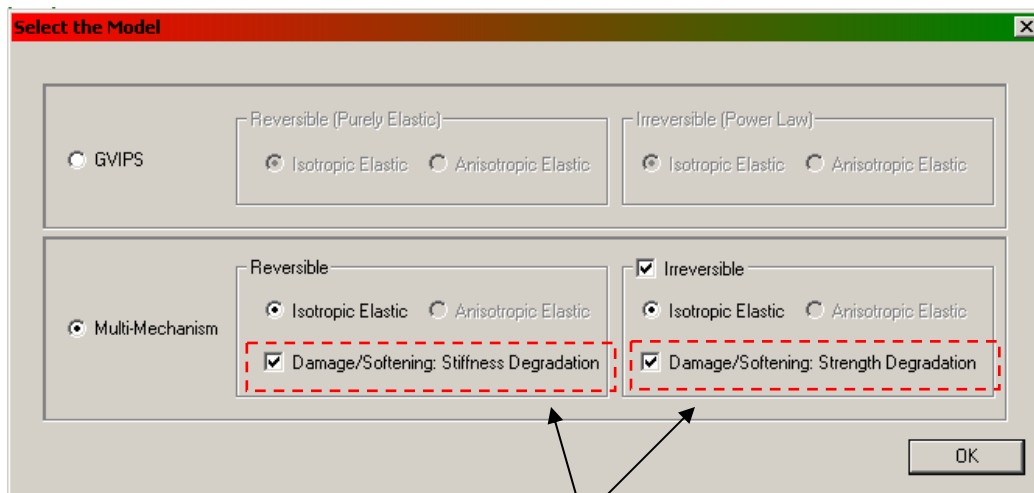
3. Numerical Testing and Documentation

The previous section presented the necessary additions to the formulation of GVIPS and the corresponding changes to the implicit integration algorithm. Another key development has been the extension of the COntstitutive Material PARAmeter Estimator (COMPARE) software to also include the damage analysis capabilities of the GVIPS model. This extension required two main components; (i) modification of the graphical user interface (GUI) of COMPARE; (ii) the derivation of the necessary damage parameter sensitivities required in the gradient-based optimization routines.

3.1 COMPARE Interface Modifications

The graphical user interface (GUI) of COMPARE was modified so that the new damage parameter data of the GVIPS model may be entered. Figures 4 to 6 show the necessary additional windows that were added. Figure 4 show's how the stiffness and strength damage options are selected, using simple checkboxes, for the GVIPS model.

Figures 5 and 6 show the new windows for entering the necessary parameters for the stiffness and strength damage, respectively. Note that there are at most four stiffness parameters while for the strength damage the window, the total number of parameters depend on the number of viscoplastic mechanisms selected.



New damage checkboxes added for stiffness and strength damage

Figure 4.—Added features in model selection of COMPARE.

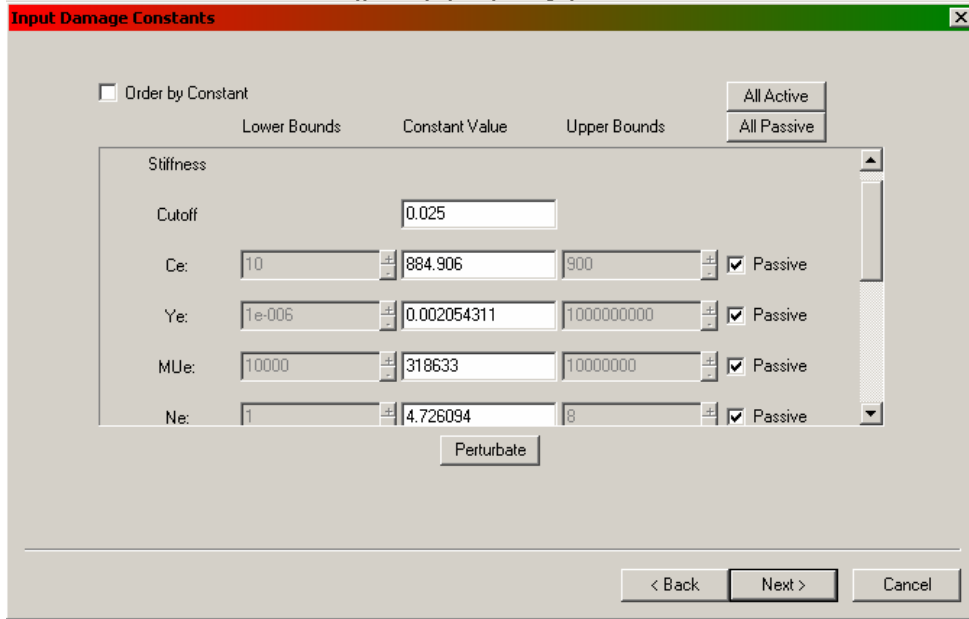


Figure 5.—Stiffness damage parameter entry window.

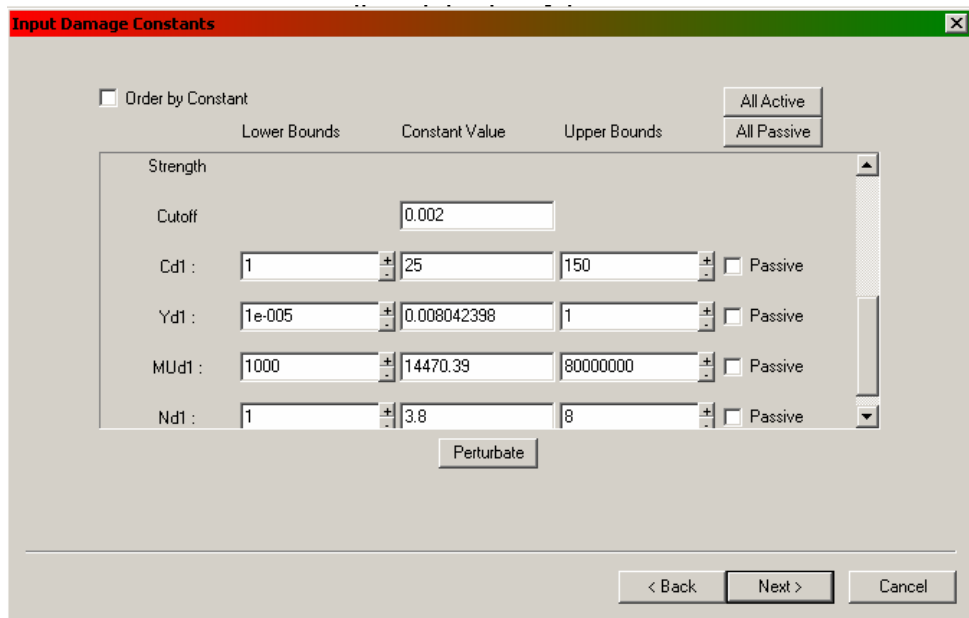


Figure 6.—Strength damage parameter entry window.

3.2 Numerical Testing

In order to test the numerical implementation of the model, an extensive matrix of tests were performed. The first set of numerical tests is used to verify the derivation and implementation of the sensitivities in COMPARE. This was accomplished using a standalone version of COMPARE in which a finite difference scheme has been implemented to evaluate the sensitivities. These simulations were run for all of the test controls, i.e., pure strain, pure stress and mixed, and for both types of damage. In all of these cases, the evolution of the sensitivities for each of the damage parameters was compared for the finite difference and the “exact” (closed-form) sensitivity expressions. Some representative results are

shown in figure 7 and 8 for the case of mixed control. Note that in both figures, the exact sensitivities compare almost exactly with that obtained by finite difference. Equally good comparisons were also obtained for the pure stress and pure strain controls. Such good correlation between the two methods of evaluating the sensitivities verifies that the derived sensitivity expressions are correct and implemented into COMPARE correctly.

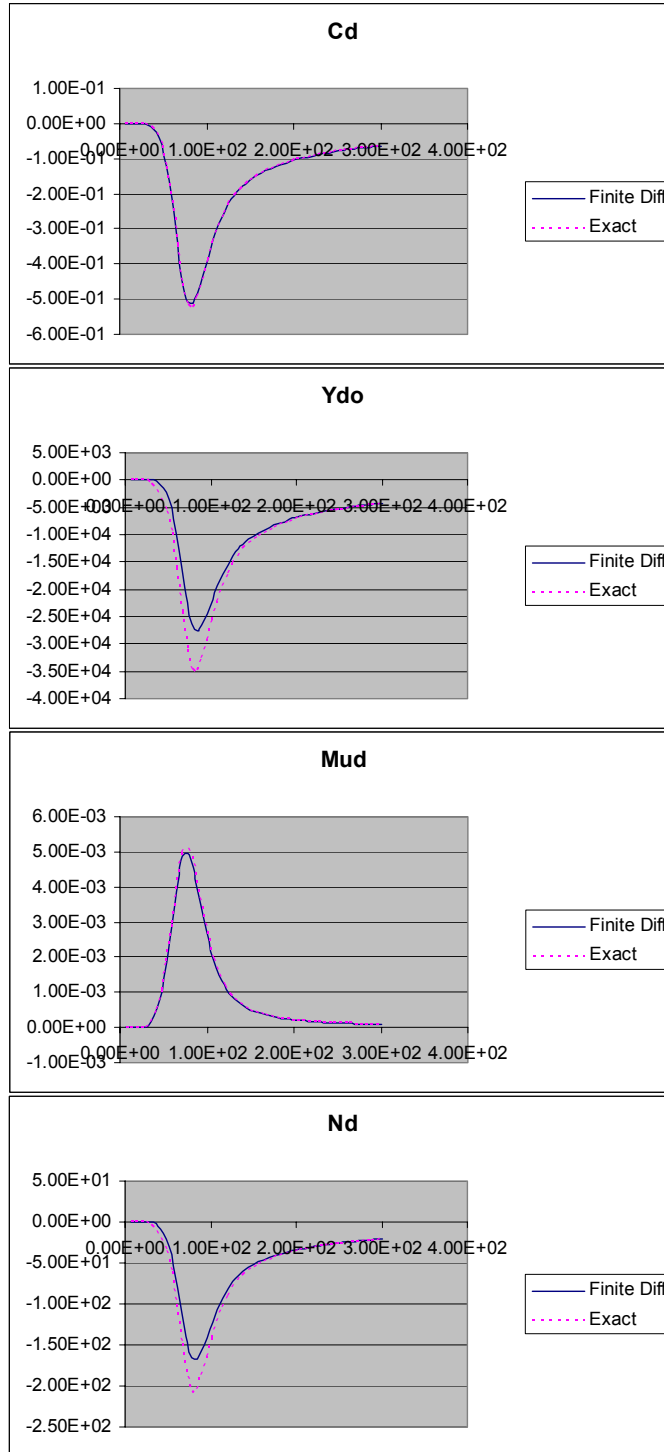


Figure 7.—Strength damage sensitivities, exact versus finite difference, mixed control.

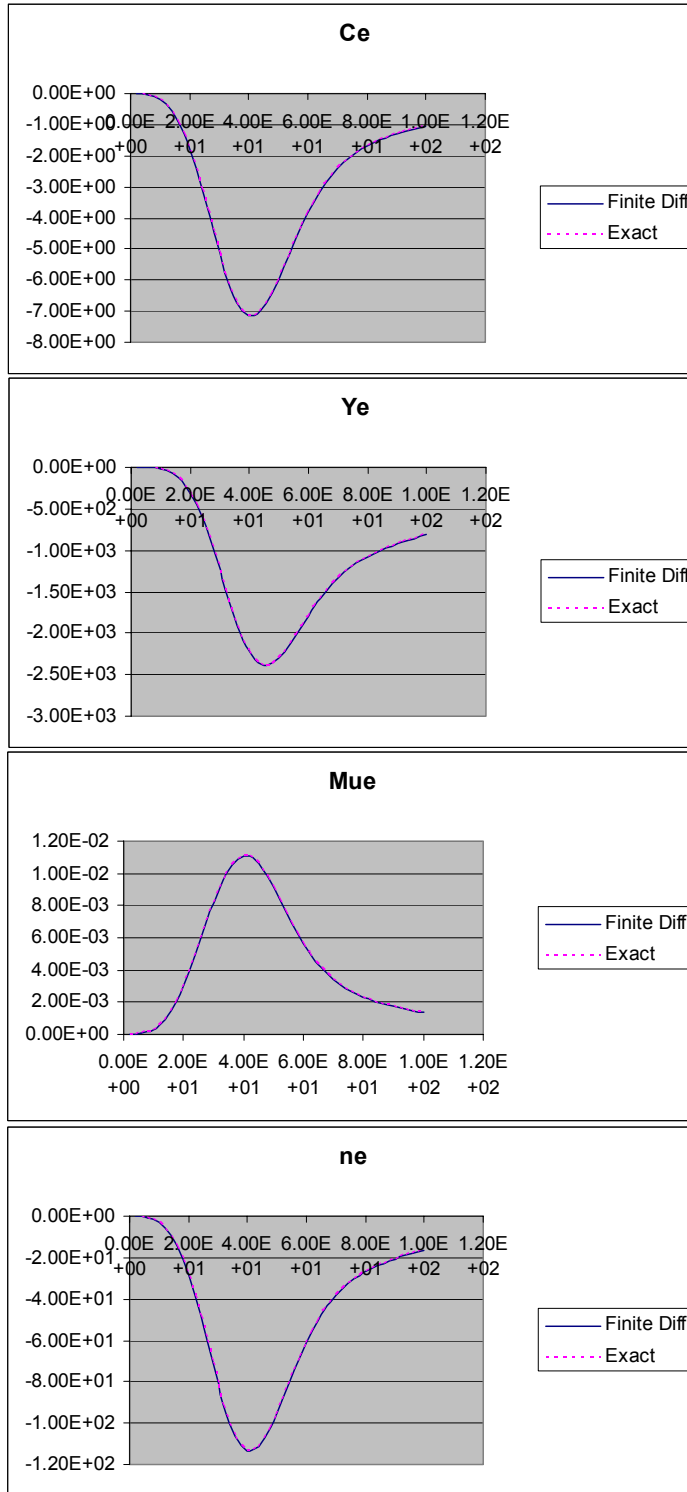


Figure 8.—Stiffness damage sensitivities, exact versus finite difference, mixed control.

Checkbox to select damage once deformation characterization is complete

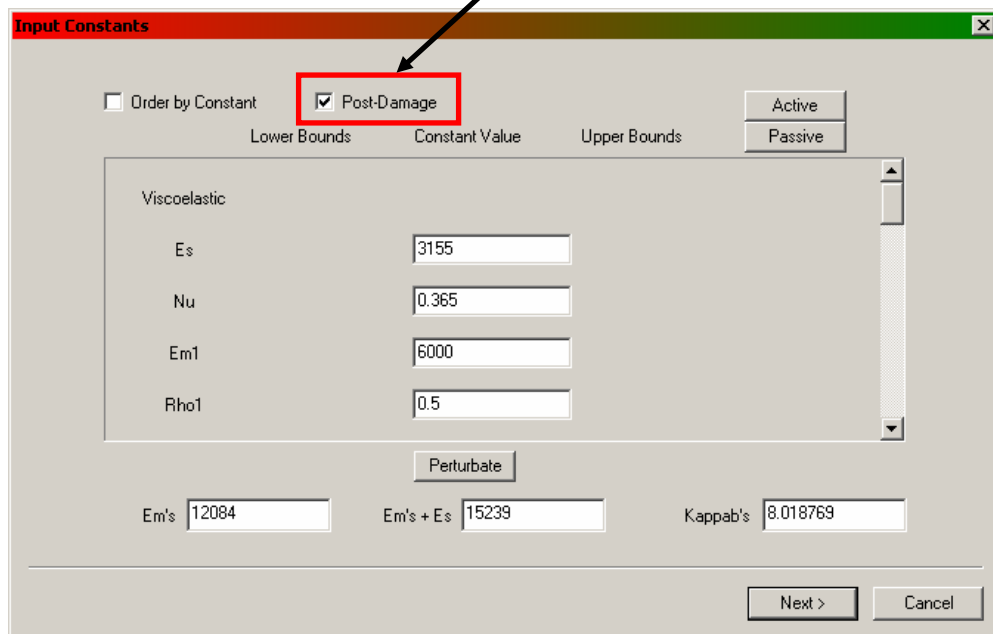


Figure 9.—Checkbox to activate damage parameter entry.

3.3 Damage Characterization of TIMETAL21S

The damage characterization process has been envisioned as a two step procedure. Specifically, we propose that the first step is the characterization of the material parameters pertaining to the deformation only response, that is, no damage effects are included in this first step.

In fact, from figure 9 we see that the COMPARE interface was designed with this process in mind. Initially, when performing the deformation phase of the characterization, the “Post-damage” checkbox is left unchecked which internally causes COMPARE to de-activate the damage analysis capabilities. Once the deformation response is characterized, the post-damage checkbox is selected and the appropriate screens (as previously shown in figs. 5 and 6) are activated and the user is now allowed to enter the damage related material parameters. In addition, now the deformation related material parameters are held passive during the characterization process. The reason for this approach is that if the complete response (both deformation and damage) is submitted to COMPARE, the program would not be able to distinguish between the deformation and damage portions of the experimental data, thus leading to an erroneous characterization of the material parameters.

In order to test the effectiveness of the proposed damage formulation and the damage characterization procedure described above, a characterization was performed on the TIMETAL21S material system. As part of the two step process, initially, the material parameters pertaining to the deformation only response were obtained in which six viscoelastic and three viscoplastic mechanisms were used, table 1. These constants were obtained from a very comprehensive characterization of TIMETAL21S using a variety of tests, i.e., three strain-controlled tensile at different rates, three creep (with data in the tests truncated so as to exclude the damage portions, tertiary creep regions, in the creep experiments), one multi-step creep, and three relaxation tests and a fully reversed cyclic deformation test. Thus the deformation behavior of TIMETAL21S was previously well established (ref. 4). Unfortunately, the corresponding damage related experimental data is very limited in that only two creep tests (15.9 and 18.9 ksi) contained tertiary creep regions which could be used for the damage characterization.

When extrapolated to the whole time durations of the creep tests, the above, deformation-only, viscoelastic-plastic model predictions are shown in figure 10, in comparison to the complete (primary/steady state/tertiary creep regions) experimental curves. Obviously there is a need for the

inclusion of material damage (softening) in the model to more closely capture the measured response. This is performed in the subsequent figures. Since the provided material parameters did not take into account the tertiary parts of the creep curves, COMPARE was used to now fit the tertiary part of available creep curves. Note that the 15.9 and 18.9 ksi creep curves are the only curves which exhibit tertiary creep.

Figure 11, shows the COMPARE results for the complete damage characterization considering both the 15.9 and 18.9 ksi tests simultaneously. This characterization used three strength damage mechanisms, which is by default, since three viscoplastic mechanisms were selected in the deformation characterization. Specific values for the strength damage parameters are given in table 2. In addition, an inelastic cut-off value of 0.047, which is not an optimized material parameter, was selected.

TABLE 1.—NASA GLENN PROVIDED VISCOELASOPLASTIC MATERIAL PARAMETERS

Parameter	Value	Parameter	Value
E_s	3155	κ_f	0.5883737
ν	0.365	n	1.017912
E_m^1	6000	μ	39711420
E_m^2	1000	κ_α^1	6.25041
E_m^3	3063	κ_α^2	4.546975
E_m^4	946	κ_α^3	6.200694
E_m^5	575	m^1	0.8
E_m^6	500	m^2	4.03071
ρ^1	0.5	m^3	7.202355
ρ^2	50.0	β^1	0.9267981
ρ^3	974.0	β^2	4.809047
ρ^4	9693	β^3	4.602119
ρ^5	14460	R^1	0.5662578
ρ^6	28128	R^2	1.548494E-7
		R^3	0.175115
		H^1	1055717
		H^2	100
		H^3	92.5475

TABLE 2.—STRENGTH REDUCTION DAMAGE PARAMETER VALUES

Parameter	Case 1 Values	Case 2 Values	Case 3 Values
$\bar{\epsilon}_{cut}^i$	0.047	0.047	0.047
C_d^1	1.09631	1.09632	1.09632
C_d^2	24.2601	29.5029	13.8935
C_d^3	7.44875	15.9741	11.7883
Y_0^1	8.16947E-005	8.16969E-005	8.16951E-005
Y_0^2	0.000443603	0.00151157	0.000198632
Y_0^3	0.000100625	0.000292666	0.000157985
μ_d^1	1.12356E+008	1.12353E+008	1.12356E+008
μ_d^2	46.664	12.1363	152.164
μ_d^3	1590.87	105.048	2542.78
n_d^1	1.0	1.0	1.0
n_d^2	1.0	1.0	1.0
n_d^3	1.0	1.0	1.0

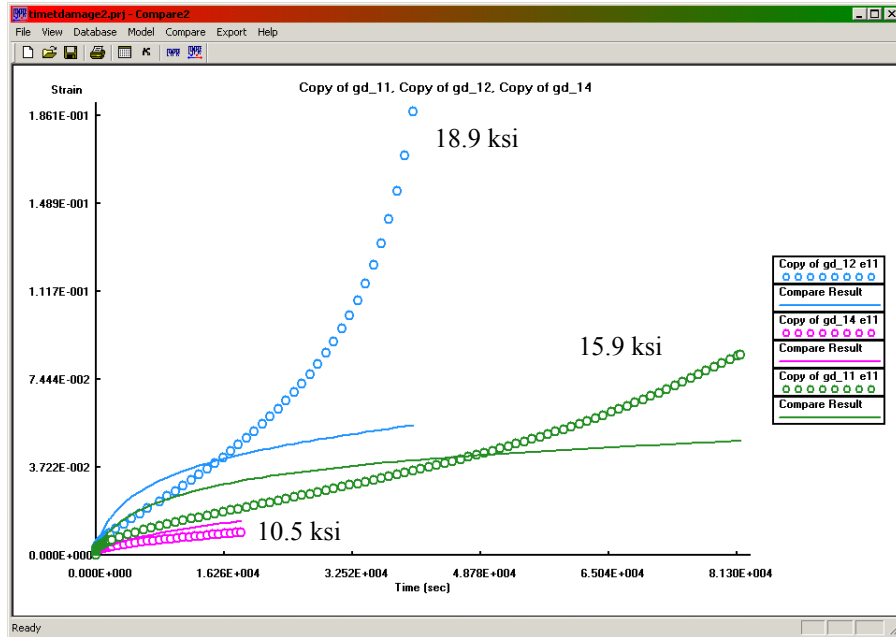


Figure 10.—Material deformation response, where the deformation-only model (no damage included) response is extrapolated for the whole creep test times.

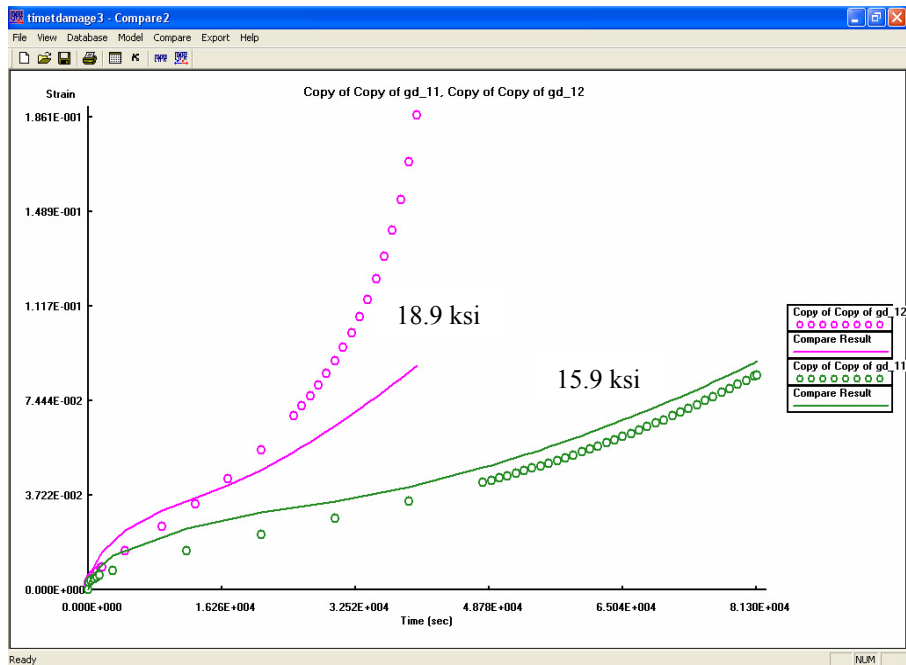


Figure 11.—Case 1: characterized tertiary creep response obtained from COMPARE.

At this point, a few comments are in order regarding the determination of the inelastic cut-off value. The inelastic strain cut-off value is a summation of the current inelastic strain vector, i.e., all of the components of the vector are included. Thus even if a plot of the inelastic (creep) strain was given, but for only a single component, you would not necessarily be able to directly (graphically) determine the value from the plot. Nonetheless, by looking at the standard creep curve using total strain versus time, one can determine a good estimate of the order of magnitude that the cut-off value should have. The approach taken here was to initially select a value around 0.05 since from figure 10 we see the tertiary creep initiates somewhere between 0.04 and 0.07 (only a single component of the total strain) and the value of 0.05 allowed sufficient tertiary creep to develop. Once COMPARE obtained an initial set of strength damage parameters, increasing or decreasing the cut-off value provided the ability to scale the accumulation of tertiary creep such that both the 15.9 and the 18.9 ksi creep curves were fit. Figure 12 shows the complete tertiary creep response which was obtained by simply extending the hold (creep) time a sufficient amount.

For demonstration purposes we performed two additional characterizations. The first characterization fit only the 18.9 ksi test and predicted the 15.9 ksi test and the second run we fit the 15.9 ksi test and predicted the 18.9 ksi test. These results are shown in figures 13 and 14. Note that even though we are only fitting a single creep curve at a time, since the deformation characterization did not fit the primary and secondary creep regions perfectly, we cannot expect the tertiary portion of the creep curve to be fit exactly. Although from figures 13 and 14, we feel the current damage formulation was able to fit tertiary part of the individual curves adequately. For these cases, the inelastic cut-off for both of these characterizations was also 0.047.

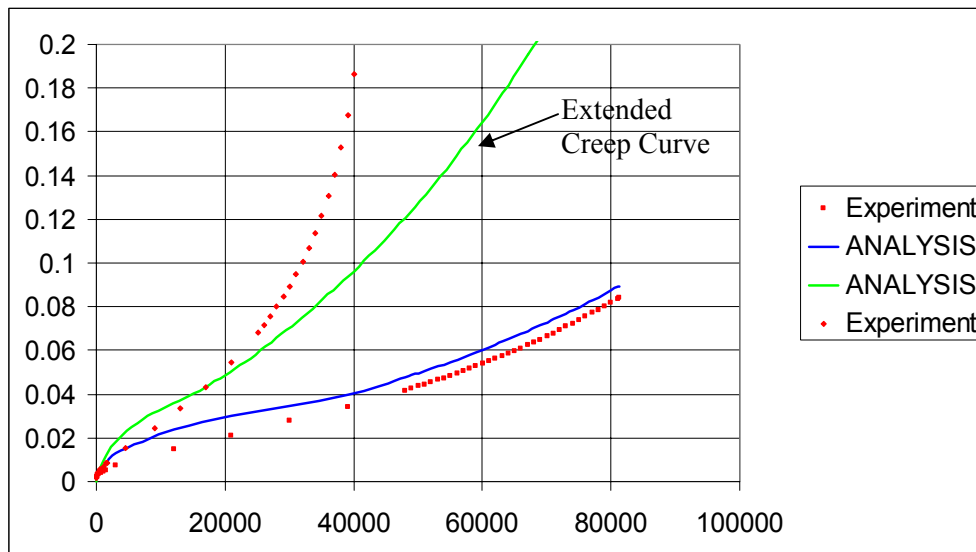


Figure 12.—Complete tertiary creep response.

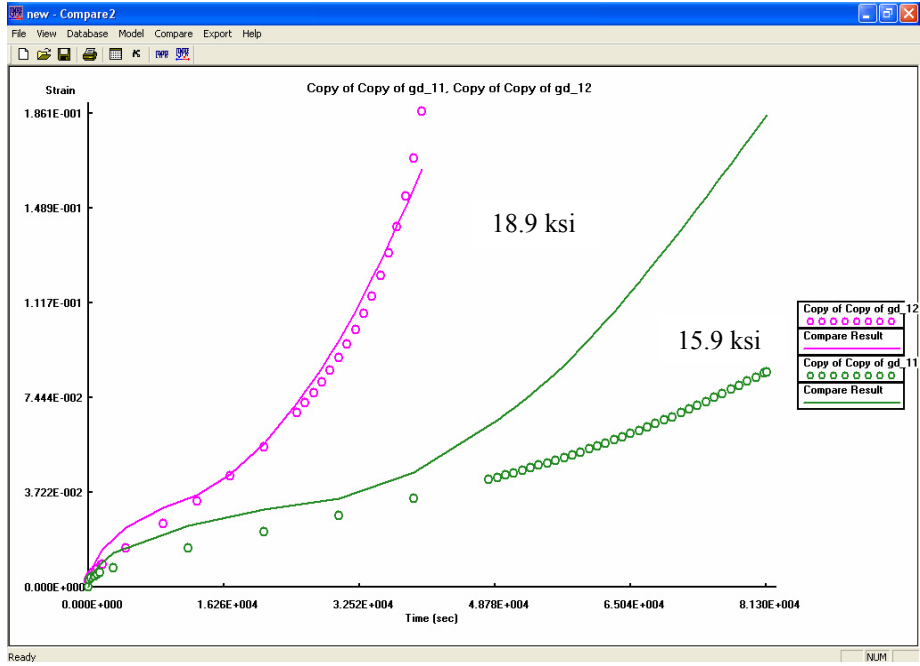


Figure 13.—Case 2: characterization of 18.9 ksi test, prediction of 15.9 ksi test.

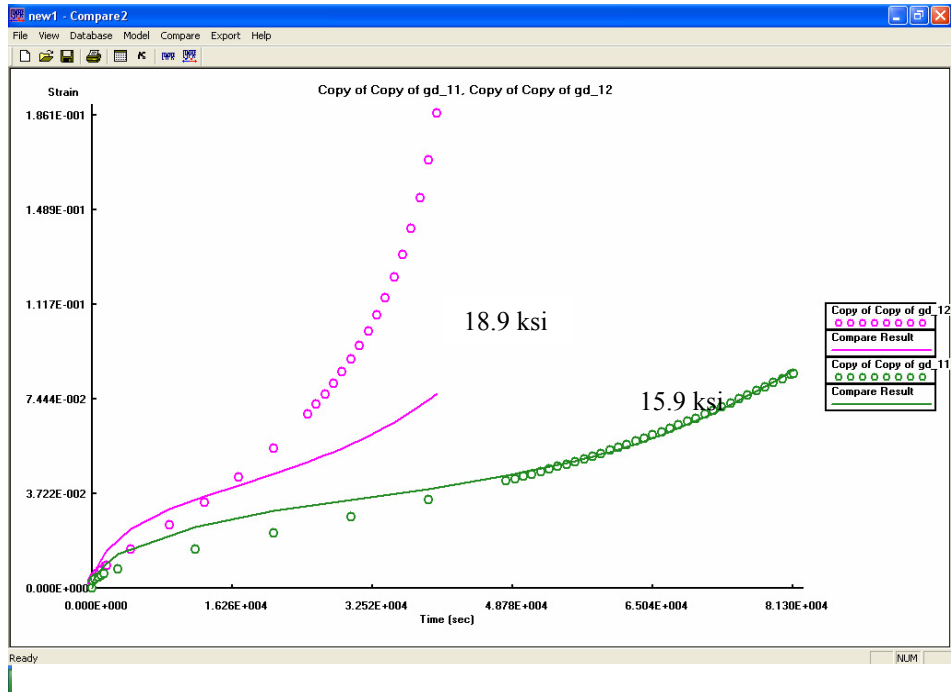


Figure 14.—Case 3: characterization of 15.9 ksi test, prediction of 18.9 ksi test.

Additionally, a second characterization was performed in which the three creep curves were characterized by themselves for both the deformation and damage response. For this characterization, the same six viscoelastic mechanisms, as shown in table 1, were used. In addition it was determined that two viscoplastic mechanisms were sufficient to fit the deformation portions of the three creep curves.

Figure 15 shows the results of the deformation characterization for the creep curves with the associated viscoplastic material parameters given in table 3. Figure 16 shows the subsequent damage characterization results obtained for an inelastic strain cut-off value of 0.05. The values of the associated strength damage parameters are shown in table 4. Again, we extended the creep hold time such that the 18.9 ksi test reached comparable failure strain as in the experiment, figure 17.

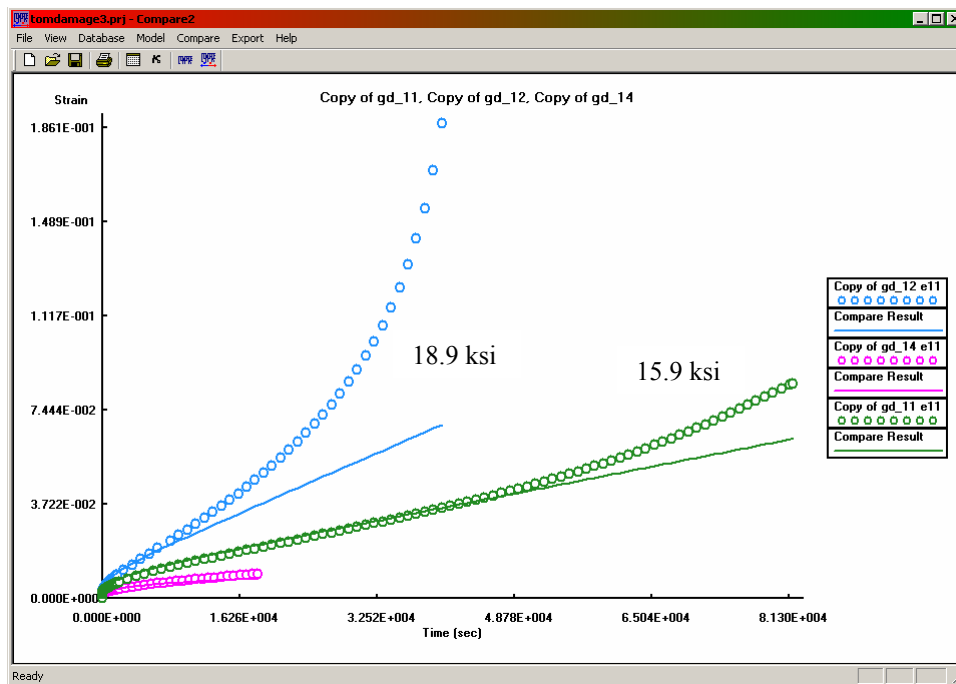


Figure 15.—Characterization of creep deformation response only.

TABLE 3.—VISCOPLASTIC MATERIAL PARAMETERS FOR CREEP ONLY FIT

Parameter	Value	Parameter	Value
κ_f	1.0	β^1	6.0
n	1.0	β^2	2.0
μ	56057190	R^1	8.61513E-3
κ_α^1	2.0	R^2	1.06271E-3
κ_α^2	6.018769	H^1	1500
m^1	2.0	H^2	1000
m^2	3.44544		

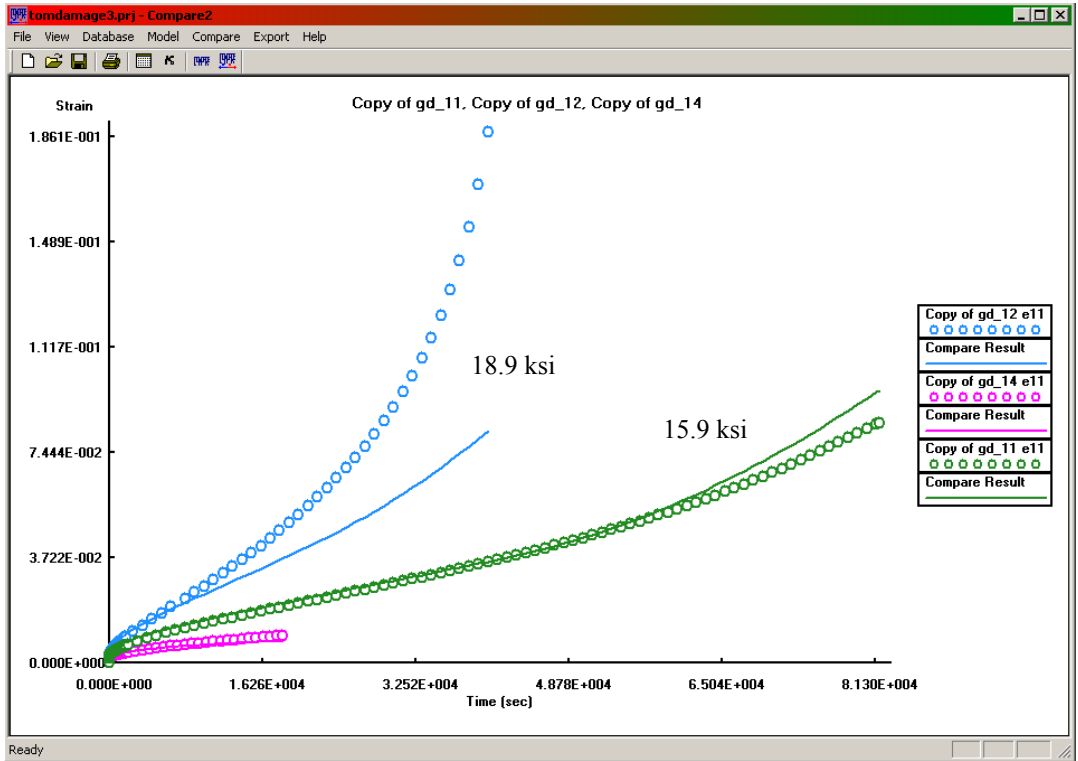


Figure 16.—Creep damage characterization from COMPARE.

TABLE 4.—STRENGTH REDUCTION MATERIAL PARAMETERS FOR CREEP ONLY FIT

Parameter	Value
$\bar{\epsilon}_{cut}^i$	0.05
C_d^1	2.065095
C_d^2	1.278901
Y_0^1	1.0E-5
Y_0^2	1.0E-5
μ_d^1	97863.39
μ_d^2	20102.58
n_d^1	2.0
n_d^2	2.0

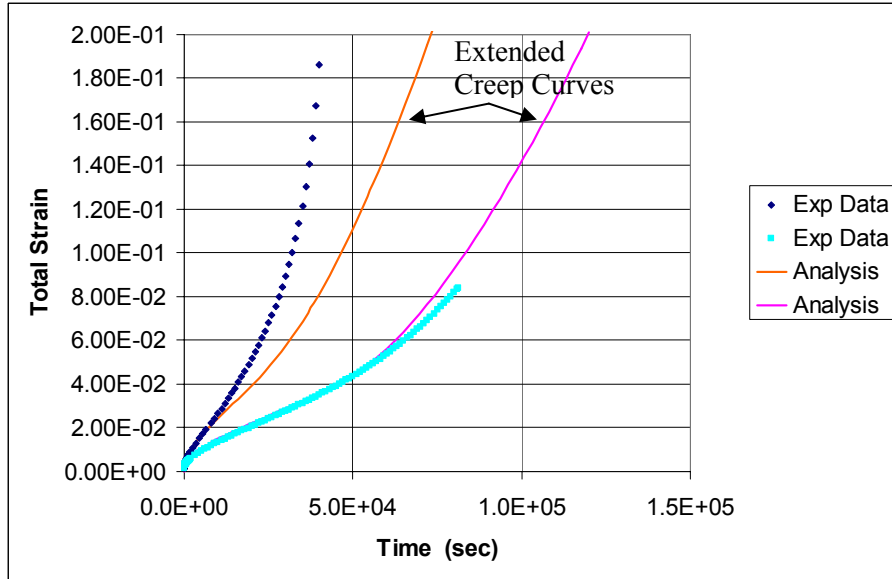


Figure 17.—Extended tertiary creep response.

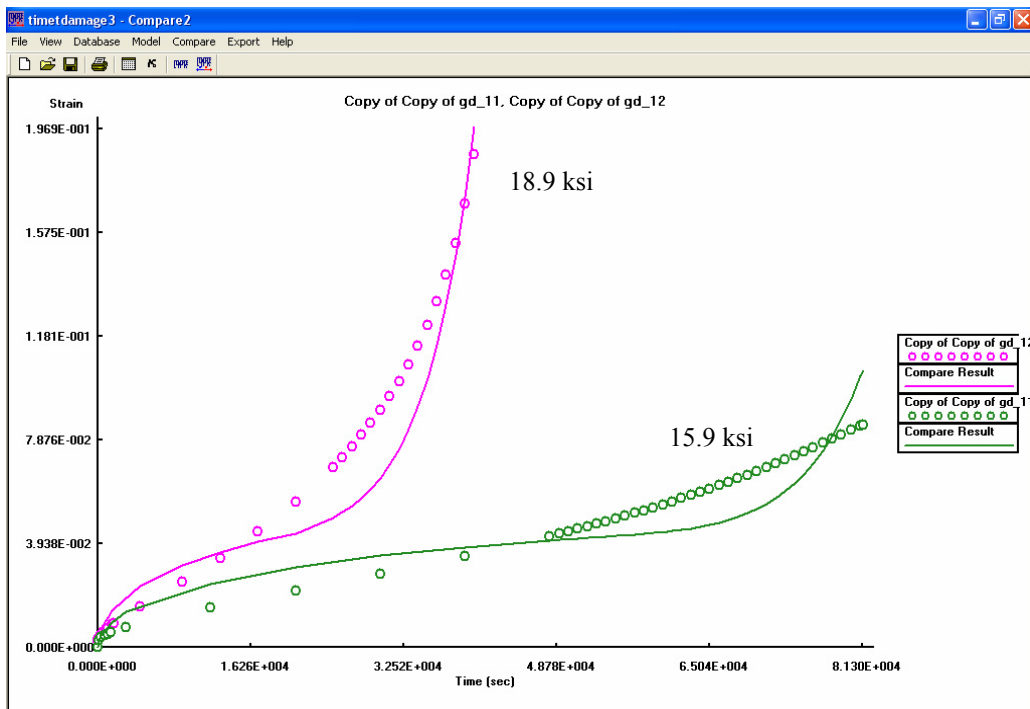
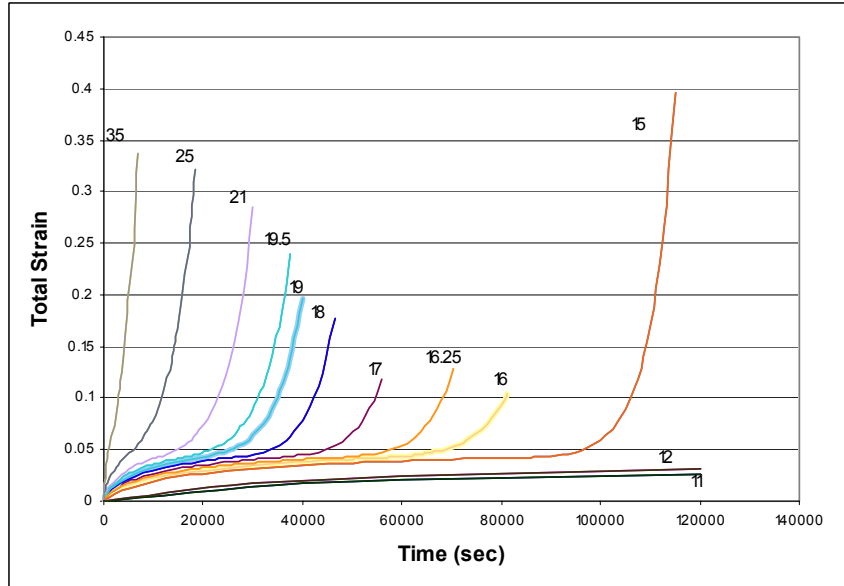
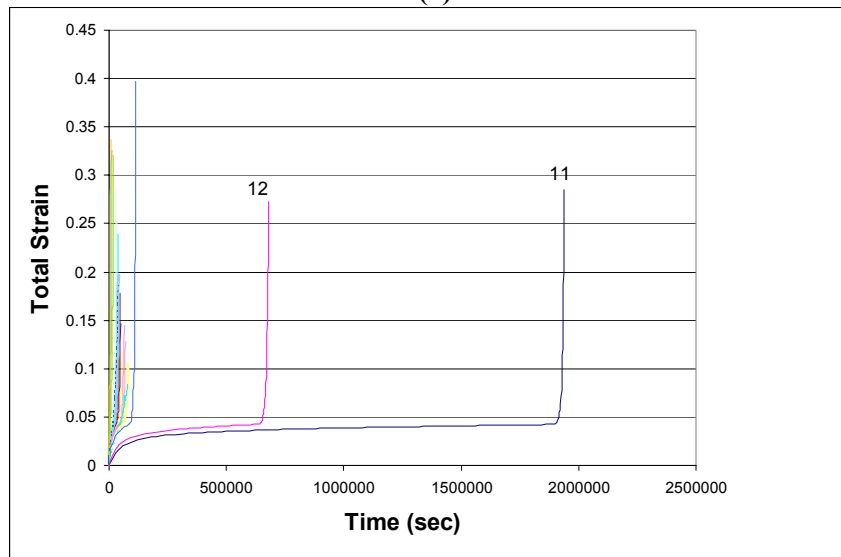


Figure 18.—Creep damage characterization using stiffness damage mechanism.

Finally, and despite the fact that the presently available experimental data for the material, TIMETAL21S, does not provide for any firm conclusion favoring a “particular” type of damage (i.e., strength and/or stiffness), we proceed next to exercise the stiffness degradation option as an alternative means for capturing the creep damage data available. To this end, we suppress any strength reduction mechanisms, and maintain all other (deformation-related) material constants as passive. The results for this exercise are shown in figures 18 and 19. Figure 19(a) and (b) show our prediction for tertiary creep curves at various stress levels (note the well-spread distributions of times-to-creep-failure indicated for the different stress magnitudes). The associated stiffness damage material parameters are given in table 5.



(a)



(b)

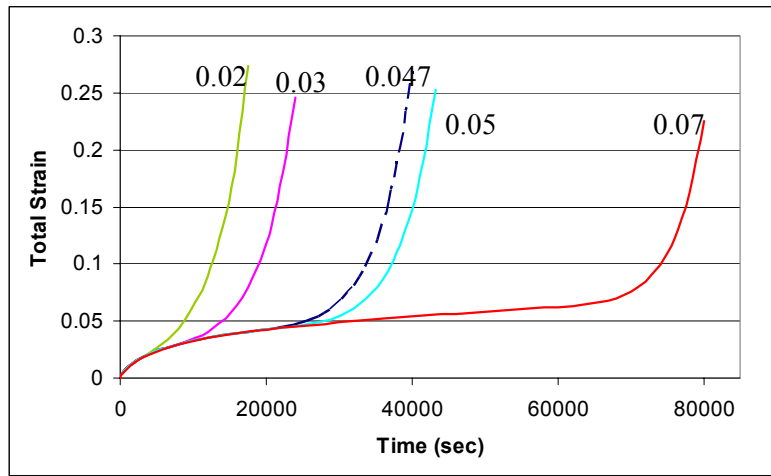
Figure 19.—Predictions of creep damage at various stress levels (ksi) using stiffness damage mechanism.

TABLE 5.—STIFFNESS DAMAGE MATERIAL PARAMETERS

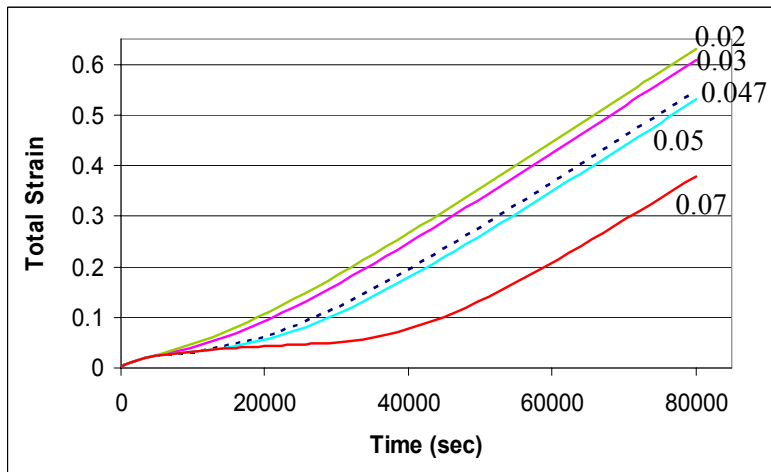
Parameter	Value
$\bar{\epsilon}_{cut}$	0.047
C_e	17.266
\bar{Y}_0	3.413E-3
μ_e	13099.62
n_e	1.0

On the basis of these results, one can conclude that either of the two damage mechanisms (stiffness only or strength only) can provide for the apparent softening in creep data. However, without further experiments, particularly upon load reversals and during load cycles, it becomes very hard to distinguish between the two softening types. This is particularly true considering that realistically both stiffness and strength degradations are conceived to interact before reaching the final failure modes of real materials.

Figures 20(a) and (b) show the effects that the cut-off value has on the tertiary creep response. Notice that increasing (or decreasing) the cut-off value basically causes the damage to occur earlier (or it is delayed). That is, the damage strain-versus time curves simply move to the left (or right).



(a) Stiffness



(b) Strength

Figure 20.—Effect of damage cut-off values for stiffness and strength damage.

3.3 Study of Limiting Cycles of Hysteresis in the Presence of Softening

From the mathematical standpoint, the coupled deformation-damage rate equations (evolution, flow, etc.) constitute a complex nonlinear dynamical system. More specifically, and borrowing terminologies from the general mathematical field of nonlinear dynamics and chaos (e.g., see ref. 7), the added complexity due to the interactions of the evolving damage mechanisms introduces an active control (nonlinear “gain” functions) character into the system, in contrast to the typical “passive” situations encountered for deformation-only modeling. For example, one may contrast the limiting state of creep strains in the steady-state regime with the “ever-changing” (continually-increasing) creep strain rates in tertiary regions, or compare the saturated stress-limited, state of plastic flow to the progressively-diminishing stresses in the softening regime under constant strain-rate conditions. Ideally, then, further insight into the understanding of the present constitutive model will be gained from the study of ensuing asymptotic/limiting behaviors under sustained with different controls (particularly cycles as in fatigue studies). A study is carried out in this section.

To start, we look at the material response for both stiffness and strength damages for the case of a cyclic stress-controlled simulation. The stress has a maximum amplitude of 50 ksi and is applied at a rate of 1 ksi/sec. Firstly, figure 21 shows the results for the case of stiffness damage. Note that the red line drawn on the figure traces the separation between the corresponding unload and reload portions of the cycle. Notice how the trend initially shows some hardening (i.e., plastic hardening) for the first three cycles, it then peaks and subsequently begins to steadily decrease (i.e., soften) as the cycles continue. This shows the competitive nature of the plastic hardening versus the stiffness damage (softening) with the stiffness damage steadily increasing until failure as expected.

Secondly, figure 22 shows the cyclic response of the material in the presence of strength damage. Again note that for the first twelve cycles we see the plastic hardening effects, but once the peak is reached and the strength reduction (softening) begins to dominate we see a drop in the curve (red trend line) with a subsequent horizontal portion signifying the residual (remaining “life”) strength state.

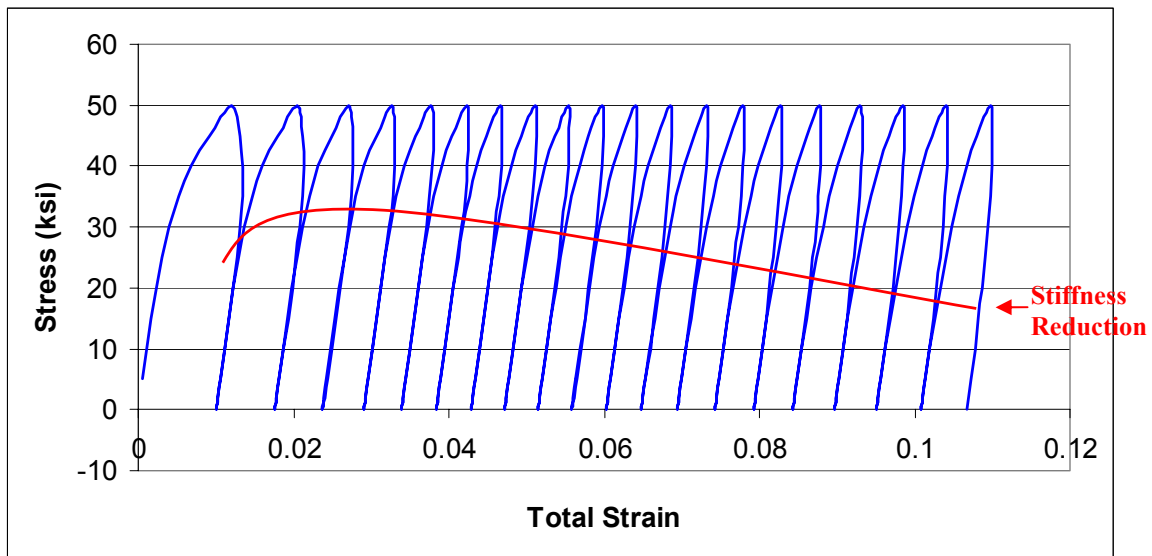


Figure 21.—Stress-control cycles with stiffness damage.

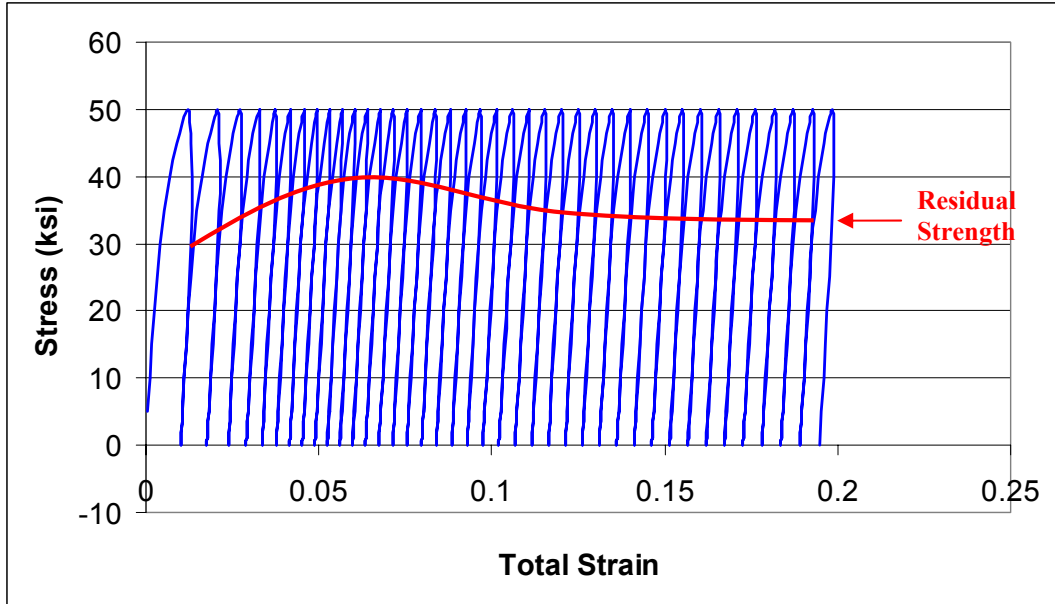


Figure 22.—Stress-control cycles with strength damage.

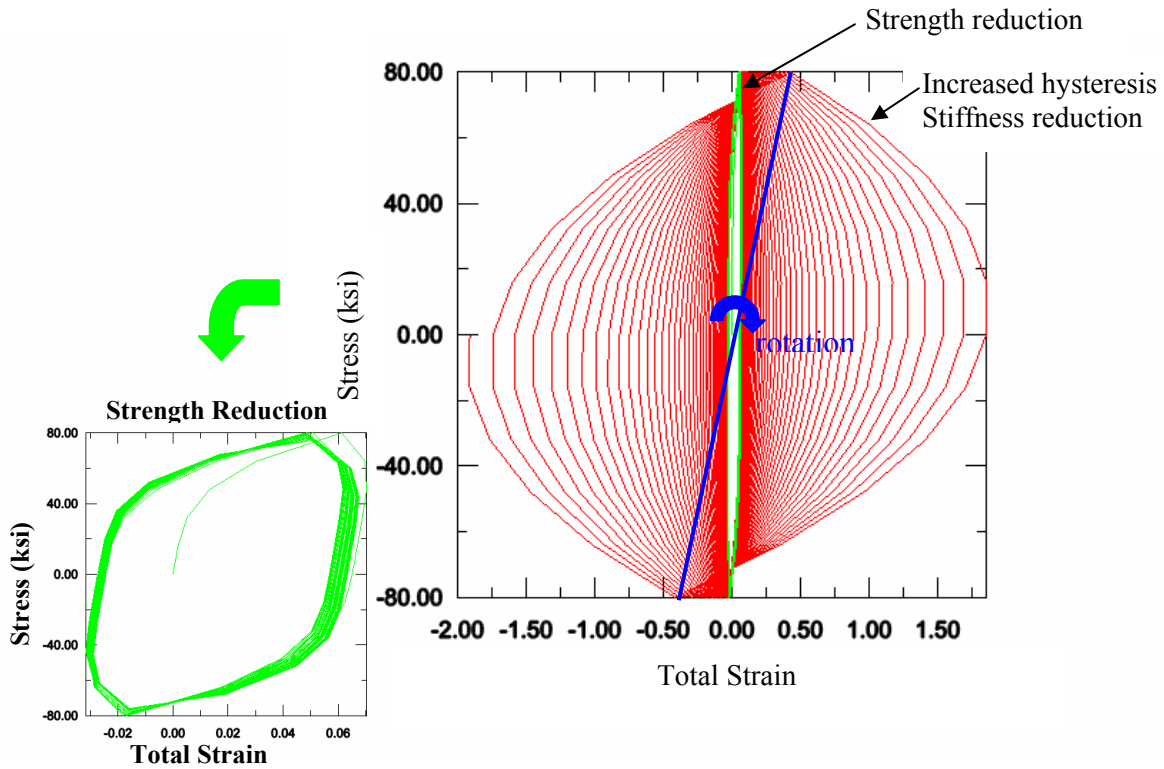
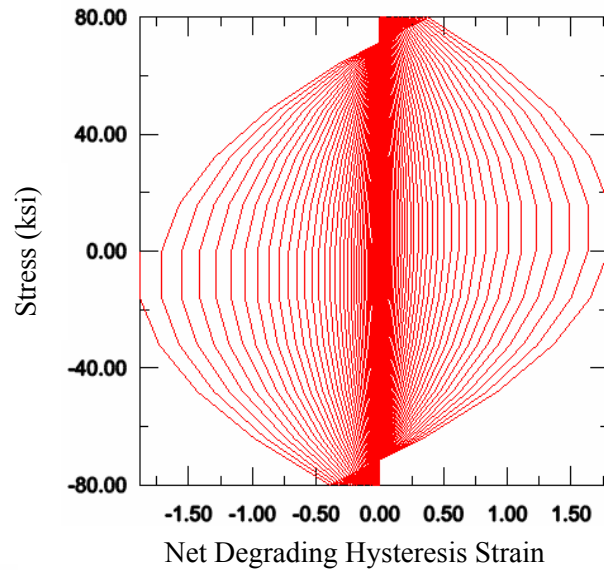


Figure 23.—Hysteresis for both stiffness and strength damage.

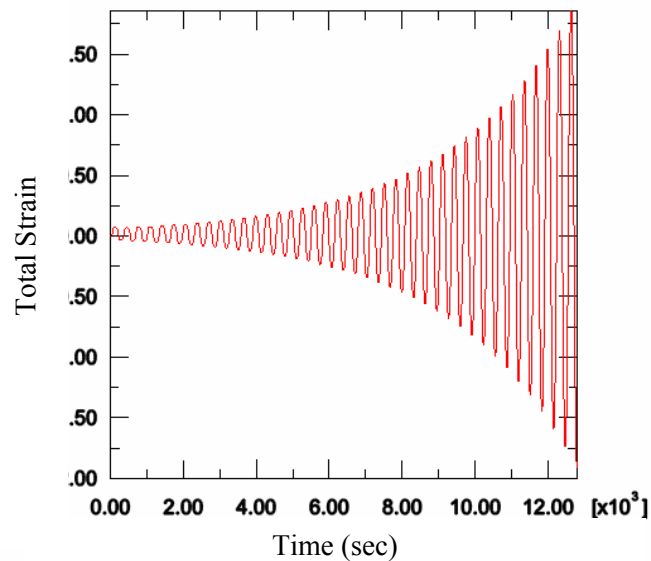
Finally in figure 23 we show the hysteretic response for the “same” material considered above when subjected to 40 fully-reversed stress-controlled cycles with a higher stress amplitude of 80 ksi at rate of 1 ksi/sec. From the figure we notice that for the case of strength reduction (green line) the slope/stiffness of the loop remains vertical (see also inset picture of strength reduction plot only). On the other hand, for

the case of stiffness damage, the resulting hysteresis loops expand and rotate (blue line) about the vertical axis, thus clearly reflecting the gradual reduction in stiffness of the material. In figures 24(a) and (b) we show the time evolution response for the stress versus nonelastic (net degrading) strains and the total strain as a function of the net degrading hysteresis strain.

In figures 25(a) and (b) we show the hysteretic plots of selected internal state variables: a) the first internal hardening state variable mechanism, $\alpha^{(1)}$, and b) the sixth non-equilibrium stress $Q^{(6)}$ mechanism. Again, note the rotation of the non-equilibrium viscoelastic stress $Q^{(6)}$.



(a)



(b)

Figure 24.—Stress hysteresis and strain evolution, stiffness damage.

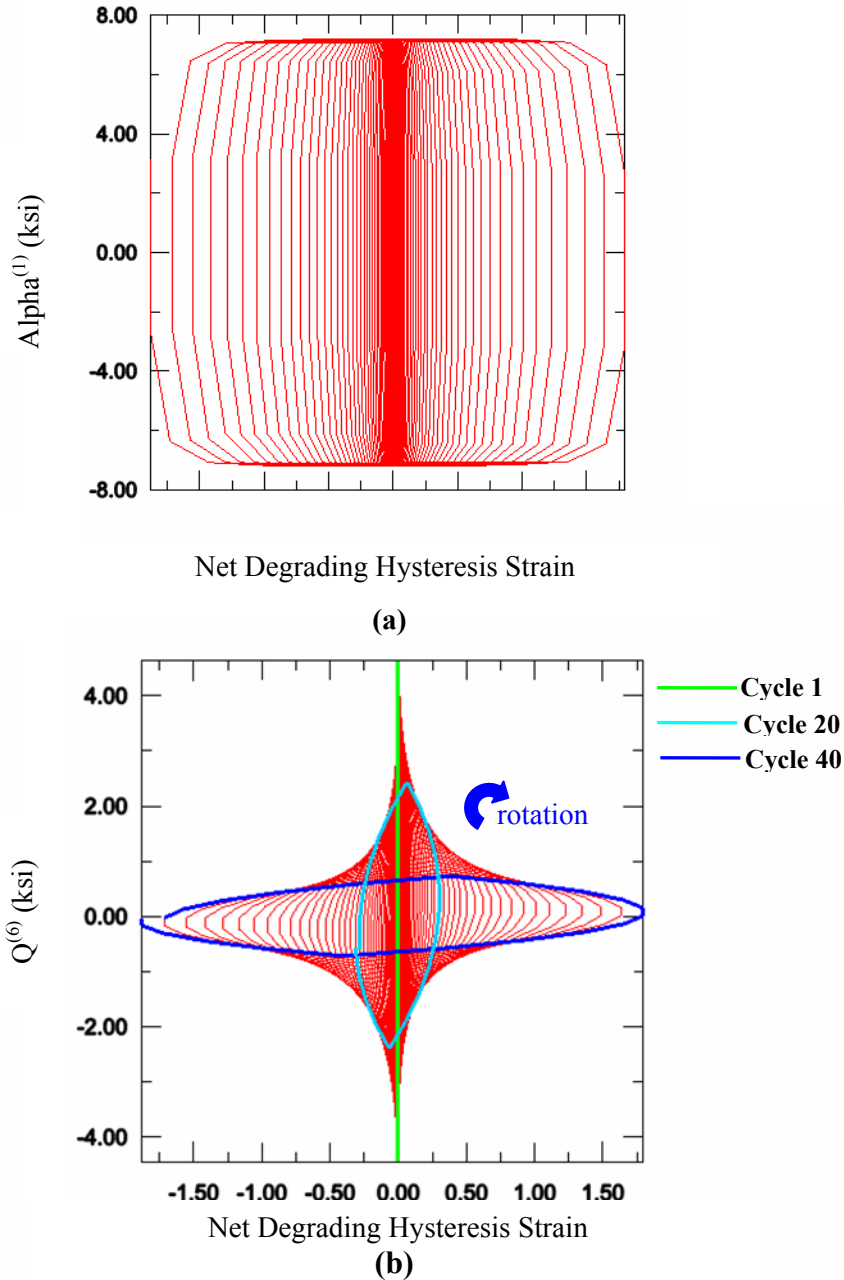


Figure 25.—Internal state variable hysteresis, stiffness damage.

Next, we consider situations involving strain controls. Figures 26 and 27 shows the hysteretic behavior of the material when subjected to 1000 strain-controlled cycles that have a strain amplitude of 0.14 at a strain rate of 2.0×10^{-3} . For the case of stiffness damage we note that at the limiting state hysteresis has reduce to almost zero stress. On the other hand we see for the case of strength damage the hysteresis will reduce to a certain level of stress and then remain constant for the remainder of the cycles.

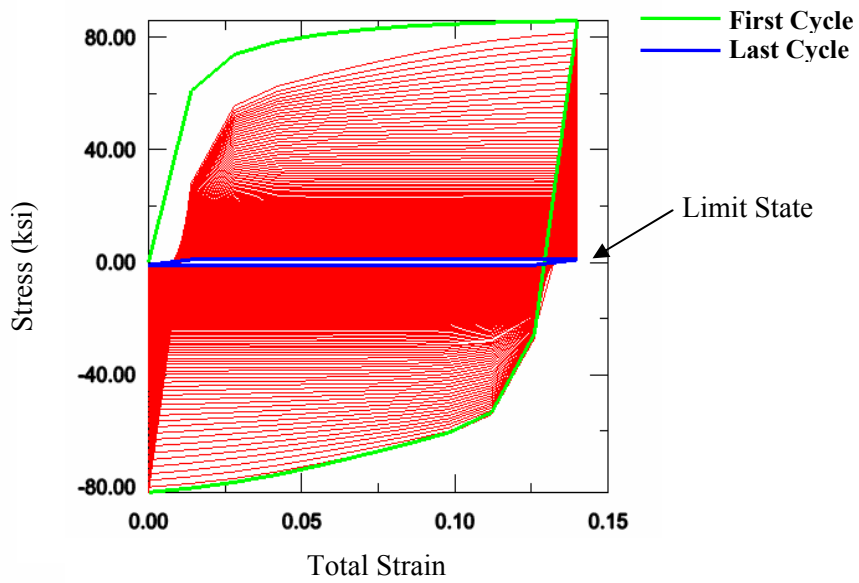


Figure 26.—Hysteretic behavior, strain-control, stiffness damage.

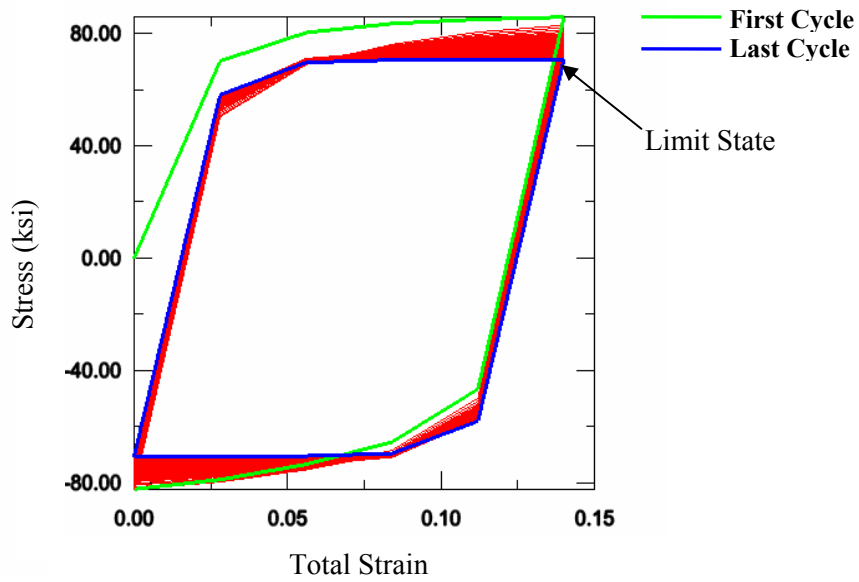


Figure 27.—Hysteretic behavior, strain-control, strength damage.

Finally, we consider a series of examples, to illustrate the effects of various loading (e.g., variable amplitude, etc.) on parameters of the hysteretic softening behavior due to stiffness damage and a combination of stiffness and strength damage. The first example is for the case of strain-controlled cyclic loading in which the strain was cycled between zero and an incrementally increasing maximum amplitude. Figure 28 shows the results for the cases of stiffness damage only and combined stiffness and strength damage. As expected, the case of combined stiffness and strength damage shows a more rapid decrease in the stress amplitude. Figure 29(a) and (b) shows the results for the case of stress-controlled cyclic loading. Notice the “rotation” of the hysteresis loops indicating the gradual decrease in stiffness, with the final loop showing an almost horizontal orientation indicating a complete loss of stiffness. Considering the case of combined stiffness and strength, figure 29(b), shows the evolution of the increasing width of the hysteresis loops for the first three stress-controlled cycles.

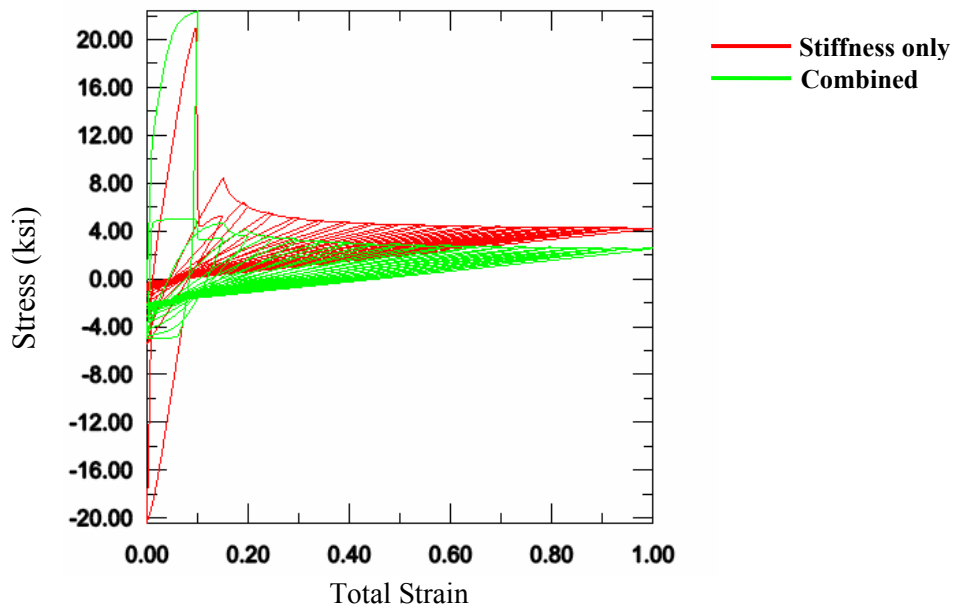


Figure 28.—Strain-controlled cyclic softening.

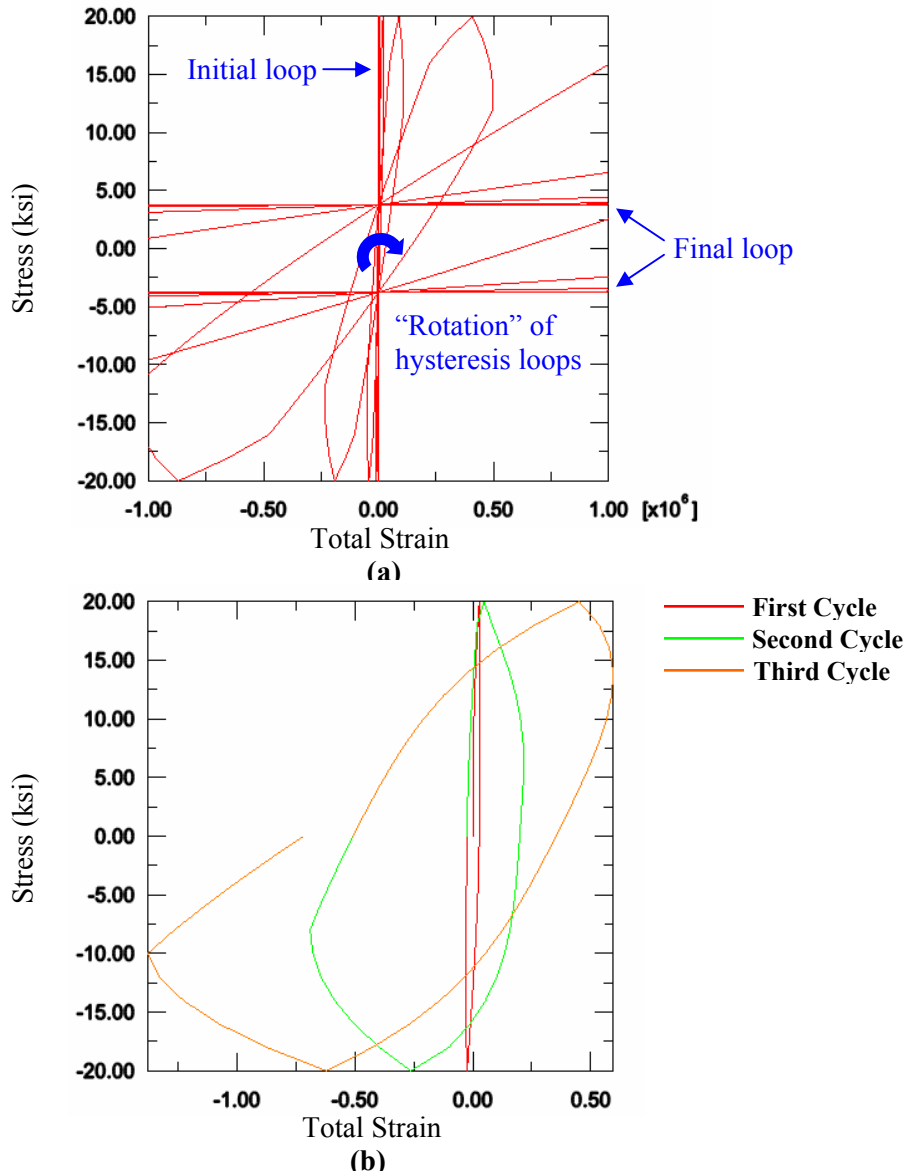


Figure 29.—Stress-controlled cycles for combined damage.

3.4 Structural Applications

With the inclusion of any type of material softening, localized regions of intense strains/strain gradients will typically occur as a precursor of any structural/component failure. It is then of utmost importance that the finite element computational model be capable of handling these situations. In particular, this calls for two very important considerations; i.e., with regard to (i) element technology and (ii) internal material length scales imbedded in the constitutive models to resolve the band details; i.e., set the proper level (intensity) and geometry (“width” and “orientation”) of the localization bands. For instance, only good finite elements and refined meshes can be used (e.g., avoid any type of locking phenomena due to shear or incompressibility constraints) and be capable of capturing bending and shear slip deformations, irrespective of the elements’ alignments relative to any ensuing localizations bands. Equally important is the ability of the material model to provide proper finite limiting sizes for the energy dissipation regions, thus ensuring the “objectivity” of the computations with respect to the final overall load – deformation response curves relative to any degree of mesh refinements.

With the above background in mind, we present a number of applications dealing with the localization phenomena, either due to strength and/or stiffness degradations in our models. Particular attention is paid to cases involving arbitrary (curved) band geometries, as well as the “uniqueness” (mesh objectivity) of the obtained load-deflection curves irrespective of the mesh size used. It is important to note that these good attributes are direct results of the several material lengths; i.e., recall the various viscous (time-dependent) terms underlying deformations and all other stiffness/strength damage mechanisms as discussed earlier. Note that this is also true whether biased (element edges paralleling the band’s directions) or unbiased meshes are utilized.

The ultimate use of any developed constitutive model will be as part of a finite element analysis. As a result the modifications to account for damage in the present GVIPS model have been included in an ABAQUS UMAT. To test the UMAT, in addition to simple test cases using a single element, larger “structural” problems of a plate with an initial imperfection were analyzed to study the phenomenon of localization. The plate has the dimensions 200 mm by 400 mm and was discretized using 800 elements, i.e., a 20 x 40 element mesh, figure 30. The initial imperfection was simulated by degrading the associated parameters for both the stiffness and/or strength damage for a single element that is located in the lower left corner. A complete summary of the material parameters, for both deformation and damage, used in these following simulations are given tables 6 to 8.

TABLE 6.—MATERIAL PARAMETERS FOR INDIVIDUAL STRENGTH LOCALIZATION SIMULATION PROBLEM

Deformation Parameters	Value	Strength Damage Parameters	Value
E_s	77000	$\bar{\epsilon}_{cut}^i$	0.02
ν	0.3	C_d	125.0
E_m^l	70000	Y_0	8.0423E-3
ρ_l	2.0	μ_d	144.70
κ_f	undamaged/damaged	n_d	3.8
	10.40/5.20		
n	3.1218		
μ	7.9269E-2		
m	1.7211		
β	5.19218		
R	1.0375E-5		
H	71818.41		

TABLE 7.—MATERIAL PARAMETERS FOR INDIVIDUAL STIFFNESS LOCALIZATION SIMULATION PROBLEM

Deformation Parameters	Value	Stiffness Damage Parameters	Value
E_s	77000	$\bar{\epsilon}_{cut}$	0.10
ν	0.3	C_e	20.0
E_m^l	0.0	\bar{Y}_0	4.0398E7
ρ_l	0.0	$\mu_e^{undamaged}$	1.2973
κ_f	undamaged/damaged	$\mu_e^{damaged}$	0.679728
	10.40/5.20		
n	3.1218	n_e	0.5
μ	7.9269E-2		
m	1.7211		
β	5.19218		
R	1.0375E-5		
H	71818.41		

TABLE 8.—MATERIAL PARAMETERS FOR COMBINED STIFFNESS
AND STRENGTH LOCALIZATION SIMULATION PROBLEM

Deformation Parameters	Value	Strength Damage Parameters	Value	Stiffness Damage Parameters	Value
E_s	77000	$\bar{\epsilon}_{cut}^i$	0.02	$\bar{\epsilon}_{cut}$	0.10
ν	0.3	C_d	125.0	C_e	200.0
E_m^l	0.0	Y_0	8.0423E-3	\bar{Y}_0	4.0398E7
ρ_1	0.0	μ_d	144.70	$\mu_e^{undamaged}$	1.2973
κ_f	undamaged/damaged	n_d	3.8	$\mu_e^{damaged}$	0.679728
	10.40/5.20			n_e	0.5
n	3.1218				
μ	7.9269E-2				
M	1.7211				
β	5.19218				
R	1.0375E-5				
H	71818.41				

Figures 31(a), 32(a), and 33(a) shows the resulting localized damage band in the plate in the presence of the different forms of damage. The corresponding history plots of the reaction force (along the edge at $x=400$) versus time is shown in figures 31(b), 32(b), 32(b). For the case of strength reduction damage, the residual strength is clearly evident from the reaction force versus time history plot shown in figure 31. On the other hand, for the cases of stiffness only, figure 32, and combined stiffness/strength damage, figure 33, note how the reaction force is completely reduced to zero.

In the final example, we have taken the same plate as described above and now applied a prescribed set of displacements simulating a punch, see figure 34. For this problem two meshes of 20x40 and 40x80 elements were used. Figure 35 shows the effective accumulated inelastic strain for both meshes. Notice that for even the coarse 20x40 mesh, once the range of the plot scale is adjusted, the distribution of the inelastic strain is remarkably close to that of the much more refined mesh. This result implies a degree of mesh insensitivity to the solution. To further demonstrate the mesh insensitivity of the solution if we look at figure 36 we see that the plots of the reaction force (calculated under the applied displacement set) versus time for both meshes are almost identical.

Considering the detailed patterns of the fully-developed failure “mode” in figures 31(a), 32(a), and 33(a), at the final residual strength state, we note the striking similarity between these and those obtained in the limit state of simple perfectly plastic materials; e.g., see (ref. 5). In fact, the obtained band configurations here are almost identical (in shape) to the so-called combined “Prandtl-Hill” mechanisms (ref. 6) obtained from slip-line theories of plasticity (ref. 5). Furthermore, note that the same similarity of these bands persists also in the case of force-control at the counterpart fully developed creep damage state (see figs. 37 and 38).

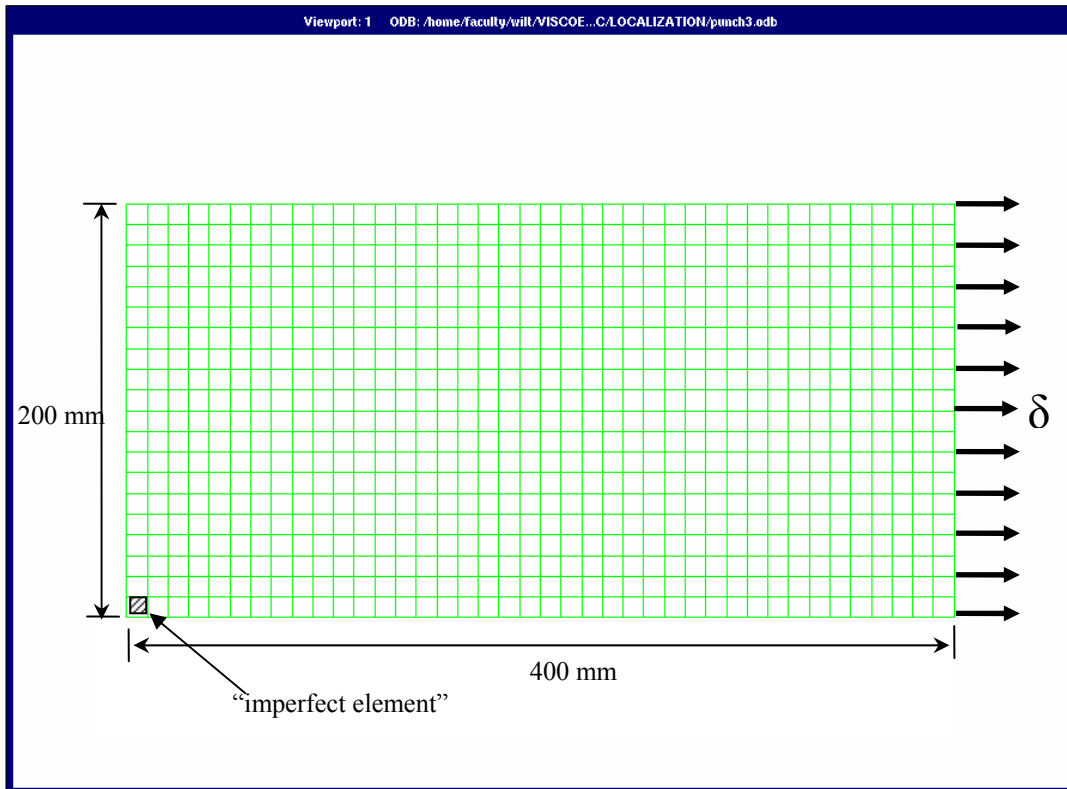
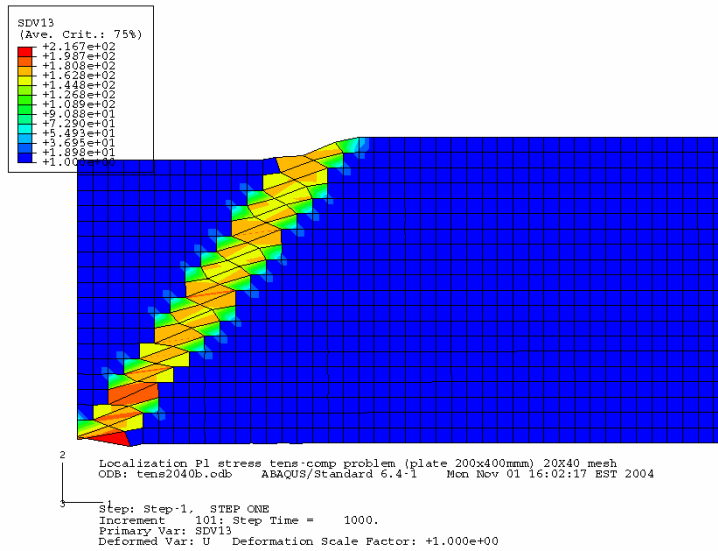
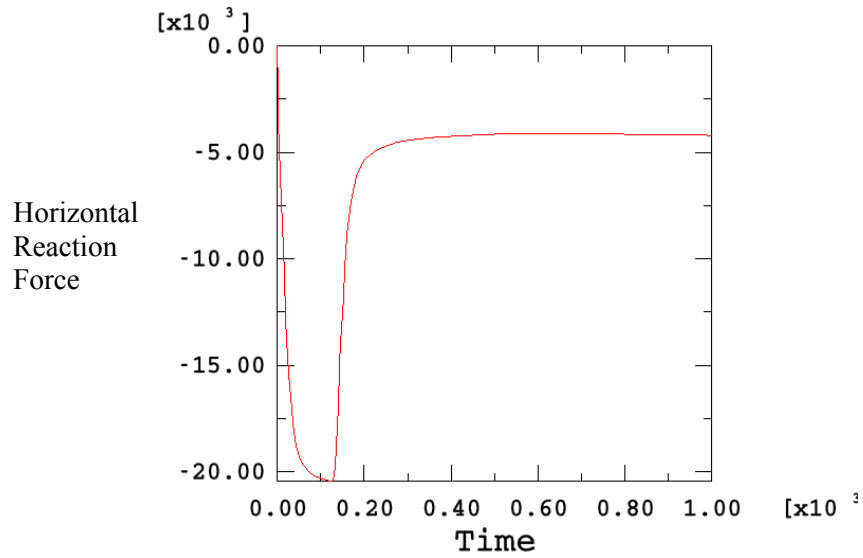


Figure 30.—Mesh for plate problem.

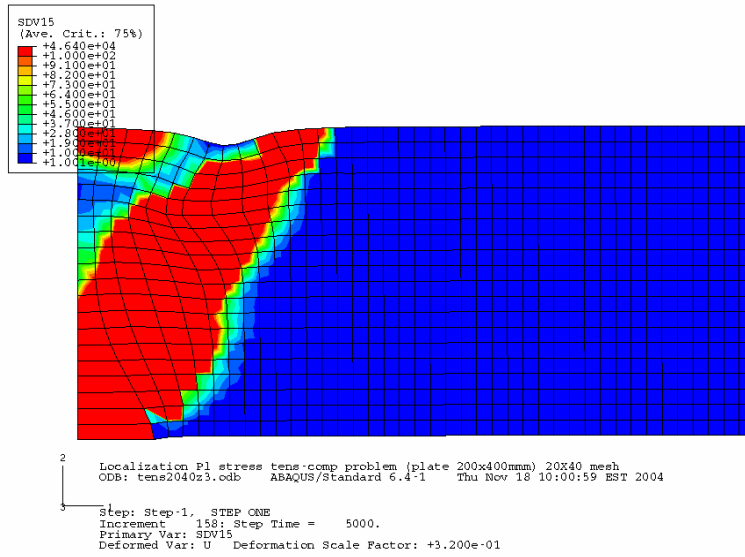


(a)

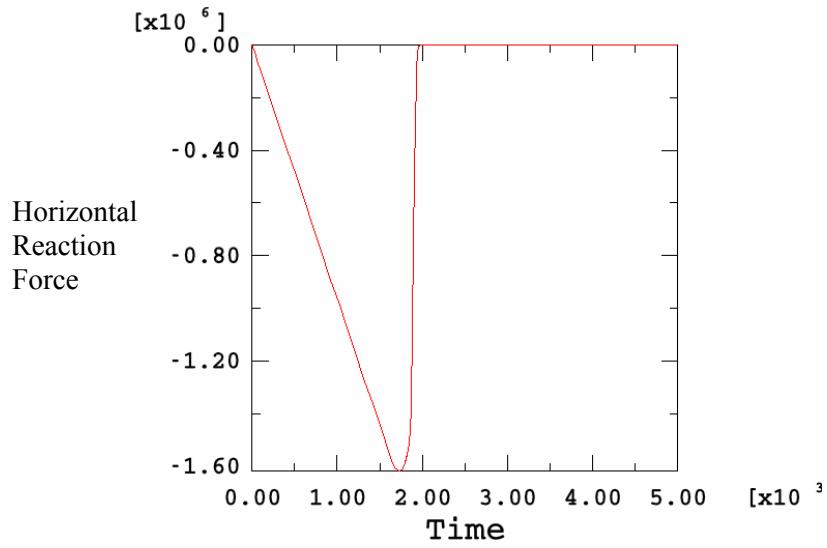


(b)

Figure 31.—Localization with strength damage only.

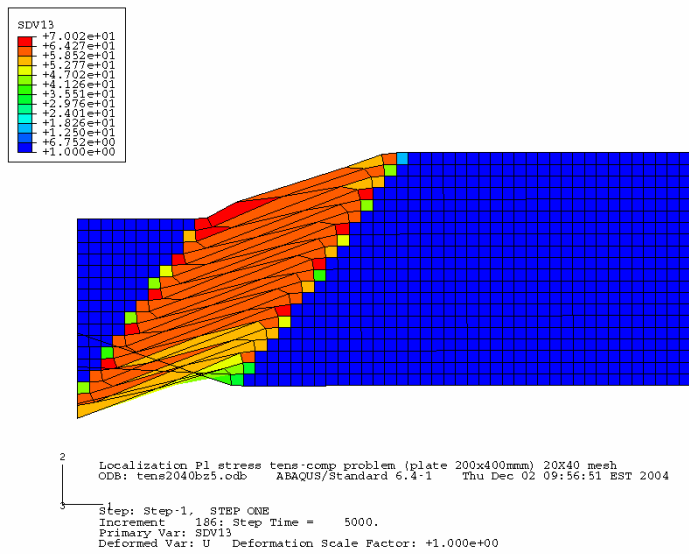


(a)

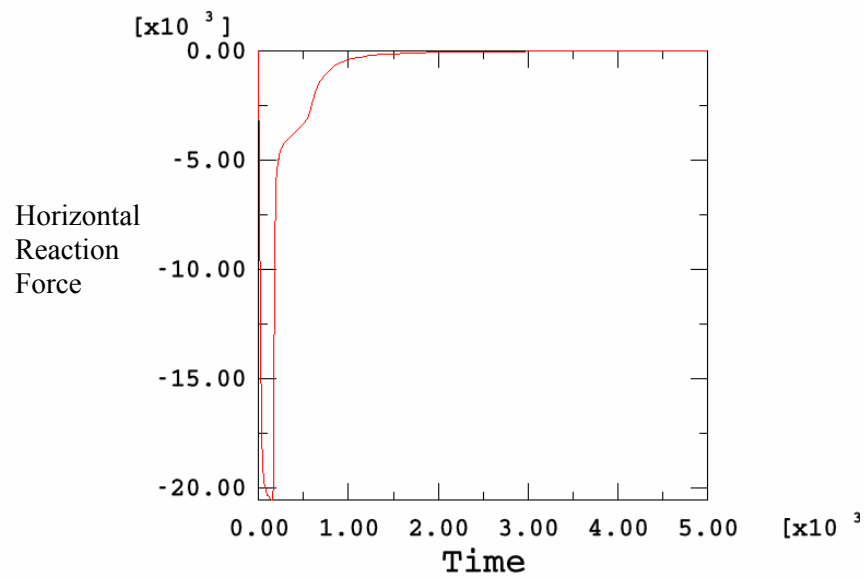


(b)

Figure 32.—Localization with stiffness damage only.



(a)



(b)

Figure 33.—Localization with combined stiffness and strength damage.

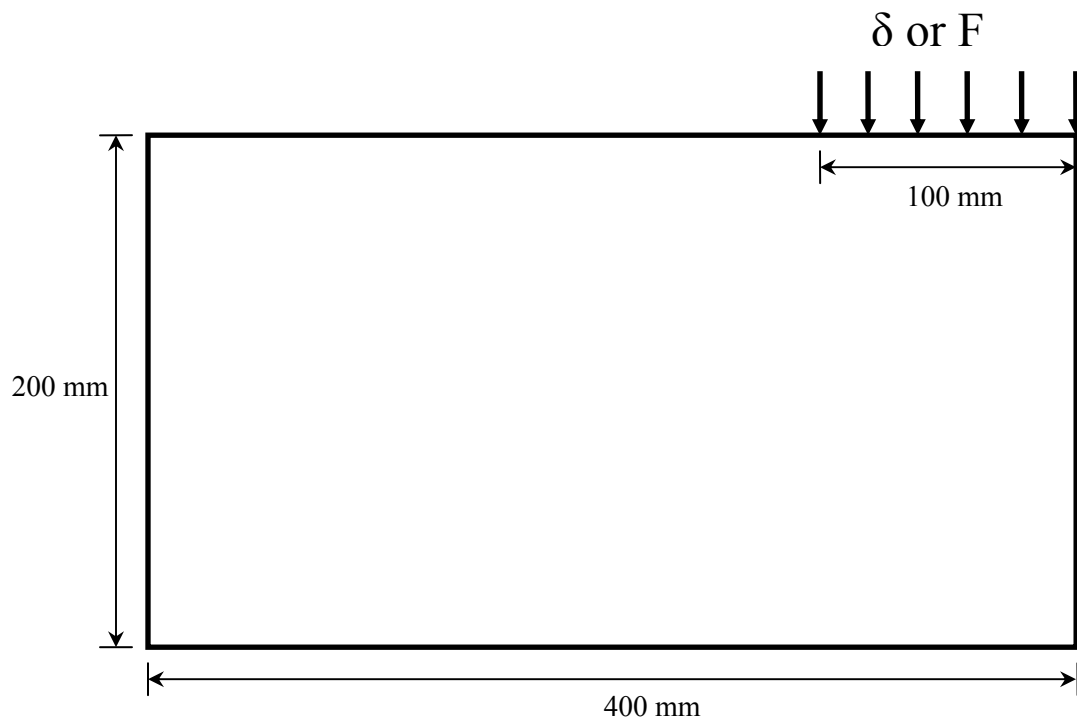
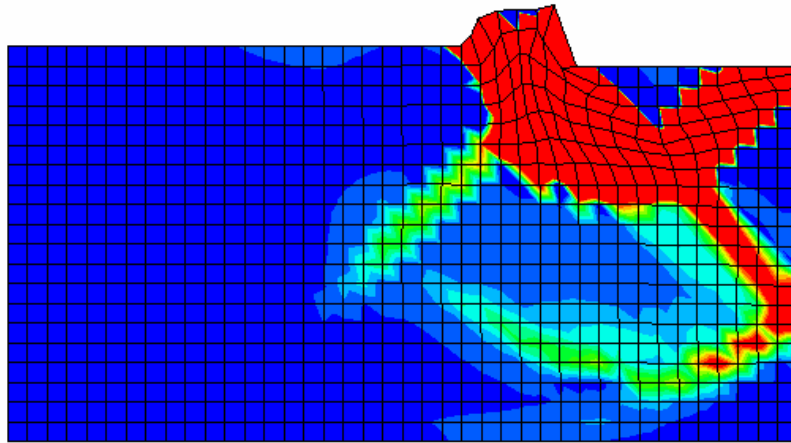
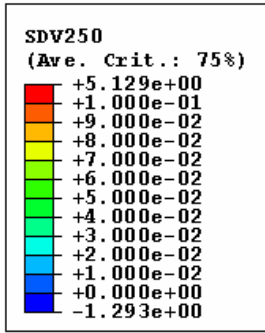
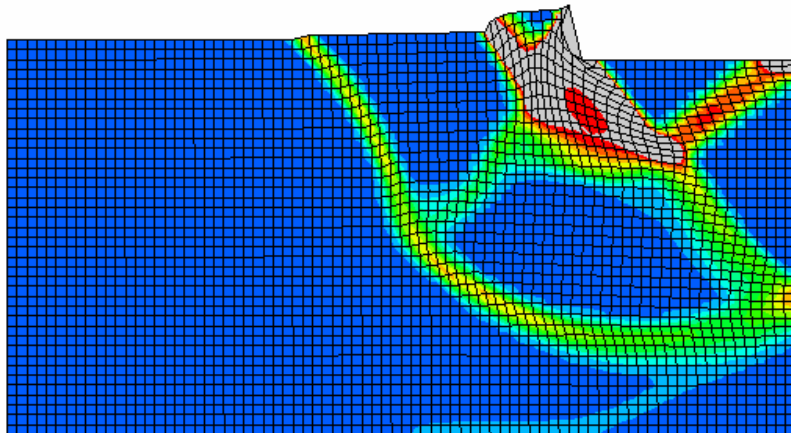
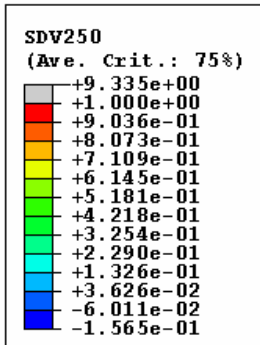


Figure 34.—Indentation problem.



2
3
1
Localization Pl stress tens-comp problem (plate 200x400mm) 20X40 mesh
ODB: punch7.odb ABAQUS/Standard 6.4-1 Tue Jan 25 18:22:07 Eastern
Step: Step-1, STEP ONE
Increment 329: Step Time = 500.0
Primary Var: SDV250
Deformed Var: U Deformation Scale Factor: +5.000e-01



2
3
1
Localization Pl stress tens-comp problem (plate 200x400mm) 20X40 mesh
ODB: punch40x80.odb ABAQUS/Standard 6.4-1 Wed Jan 26 15:20:20 East
Step: Step-1, STEP ONE
Increment 381: Step Time = 500.0
Primary Var: SDV250
Deformed Var: U Deformation Scale Factor: +5.000e-01

Figure 35.—Displacement control, indentation simulation for 20x40 and 40x80 meshes, inelastic strain distribution.

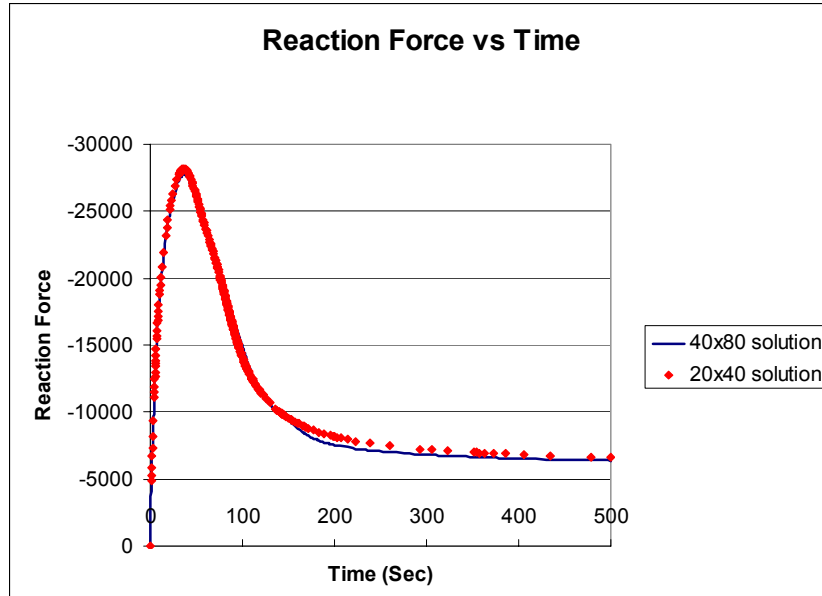
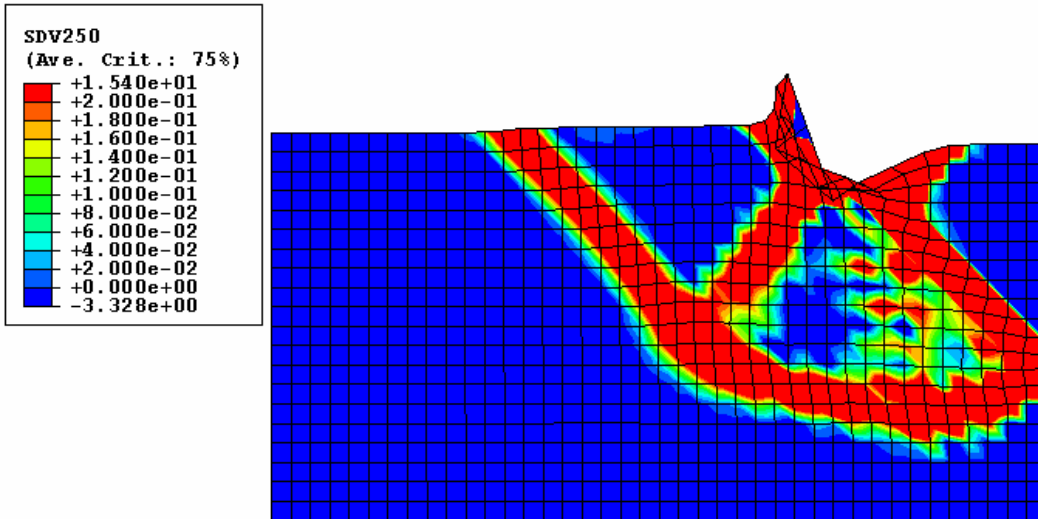


Figure 36.—Comparison of force versus time curves for both meshes.

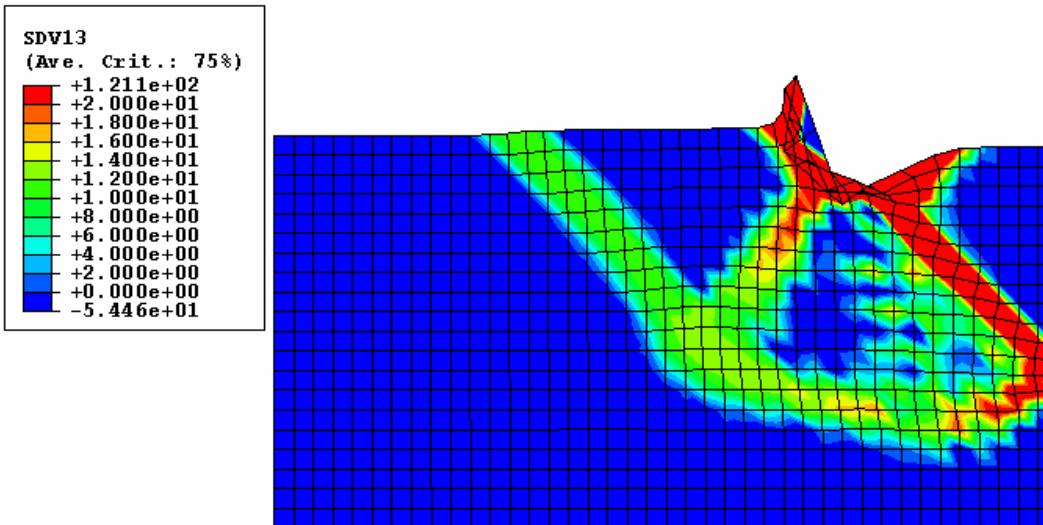
The applications presented above were performed under displacement control conditions. The primary reason for this is to allow the full peak to post-peak response of the structure to be analyzed. On the other hand, if force control was used, only the structural response to the peak of the force displacement history could be produced. Anything post-peak under load control is known to be inherently unstable. Nonetheless, since the present damage model is fully-coupled with the solution procedure, whether the analysis is performed under load or displacement control identical results up to the peak would be obtained. Furthermore, and although the situation here is more complex, one can recall the simple theoretical arguments in connection with limit analysis theorems (e.g., see refs.5 and 6) for perfectly-plastic structures; i.e., when a path-to-failure exists, the structure will find it and thus will not stand up, irrespective of the particular control mode (for displacements or conjugate forces). One therefore anticipates that, for the present rate-dependent case, and given sufficient time under constant “conjugate” forces, similar failure mode (and associated localization morphology), as the one reached through displacement-control, would be obtained.

A specific example is given below to demonstrate this remarkable, and practically important, fact in the context of the softening models formulated here. In particular, it is once more shown that the final failure mode reached is “unique” irrespective of the mesh used to resolve the localization details, and the same is also true for the resulting critical times-to-failure, obtained. Note that many other alternative damage constitutive models in the available literature (e.g., stress-based, strain-based, etc.) would fail these “uniqueness” and “objectivity” tests under either force- or displacement-controls.

Specifically, figures 36 and 38 show the distribution of the accumulated inelastic strain and the strength damage parameter for the coarse (20x40) and refined (40x80) meshes, respectively. It is quite remarkable that for both meshes, under this case of force control, the localization bands produced exhibit almost identical patterns. Please note that times at which these comparable localization patterns were produced were at 3075 sec for the coarse mesh and 3000 sec for the refined mesh which is a difference of only 75 sec (i.e., 2.4 percent), in addition, from the color scale we see that the maximum accumulated inelastic strains are 15.4 for the coarse mesh versus 14.39 for the refined mesh which is quite remarkable. Finally, a global measure of the structural response for this case of force control is presented as the displacement of the node located at the line of symmetry versus time, figure 39. As expected, we see a significant acceleration of the displacement as complete structural failure is approached.

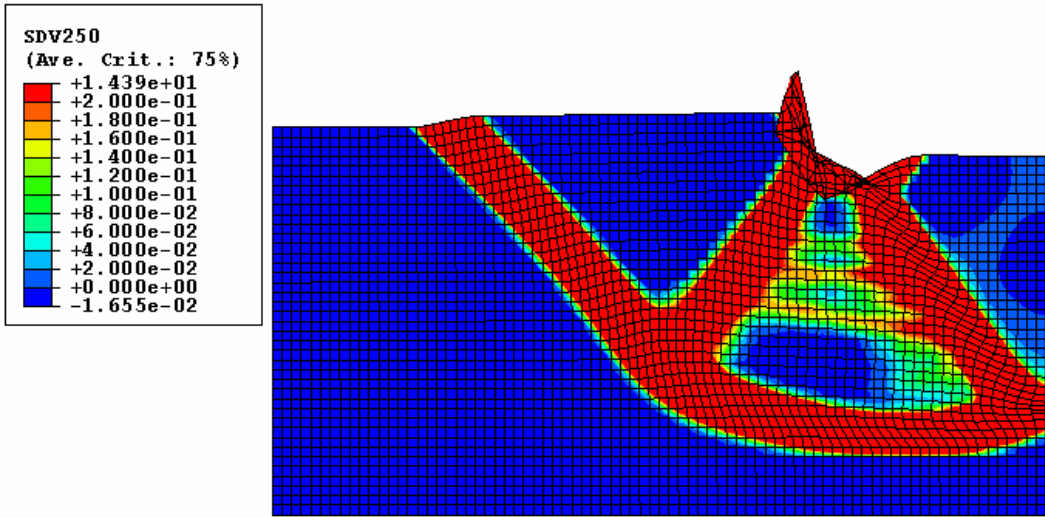


2
 3—1
 Localization Pl stress tens-comp problem (plate 200x400mm) 20X40 mesh
 ODB: punch7sig3.odb ABAQUS/Standard 6.4-1 Sat Feb 19 08:35:03 East
 Step: Step-1, STEP ONE
 Increment 219: Step Time = 3075.
 Primary Var: SDV250
 Deformed Var: U Deformation Scale Factor: +4.977e-01
Inelastic Strain Distribution



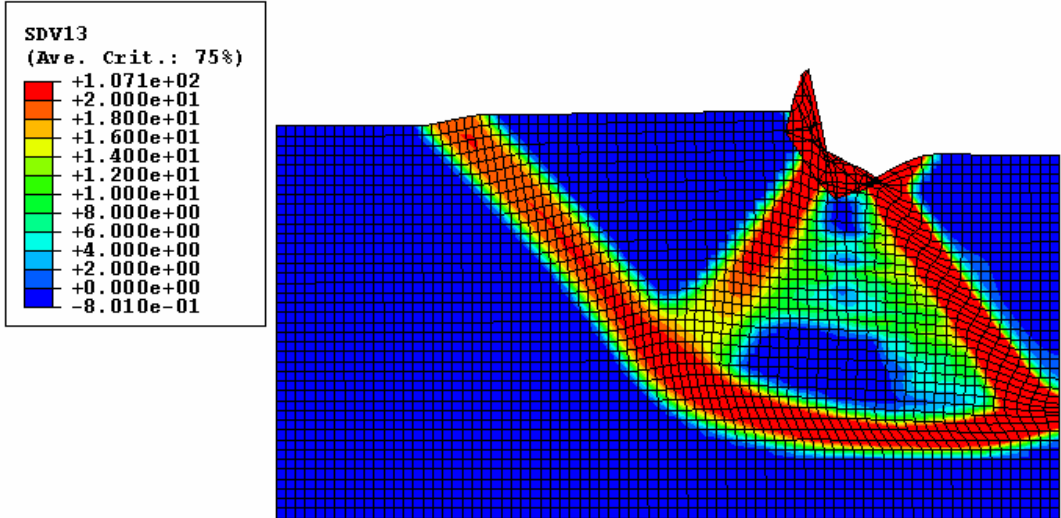
2
 3—1
 Localization Pl stress tens-comp problem (plate 200x400mm) 20X40 mesh
 ODB: punch7sig3.odb ABAQUS/Standard 6.4-1 Sat Feb 19 08:35:03 East
 Step: Step-1, STEP ONE
 Increment 219: Step Time = 3075.
 Primary Var: SDV13
 Deformed Var: U Deformation Scale Factor: +4.977e-01
Strength Damage Distribution

Figure 37.—Load control: damage localization 20x40 mesh.



2
 | Localization Pl stress tens-comp problem (plate 200x400mm) 20x40 mesh
 ODB: punch40x80sig.odb ABAQUS/Standard 6.4-1 Mon Feb 21 19:52:51 E
 3—1
 Step: Step-1, STEP ONE
 Increment 363: Step Time = 3000.
 Primary Var: SDV250
 Deformed Var: U Deformation Scale Factor: +5.757e-01

Inelastic Strain Distribution



2
 | Localization Pl stress tens-comp problem (plate 200x400mm) 20x40 mesh
 ODB: punch40x80sig.odb ABAQUS/Standard 6.4-1 Mon Feb 21 19:52:51 E
 3—1
 Step: Step-1, STEP ONE
 Increment 363: Step Time = 3000.
 Primary Var: SDV13
 Deformed Var: U Deformation Scale Factor: +5.757e-01

Strength Damage Distribution

Figure 38.—Load control: damage localization 40x80 mesh.

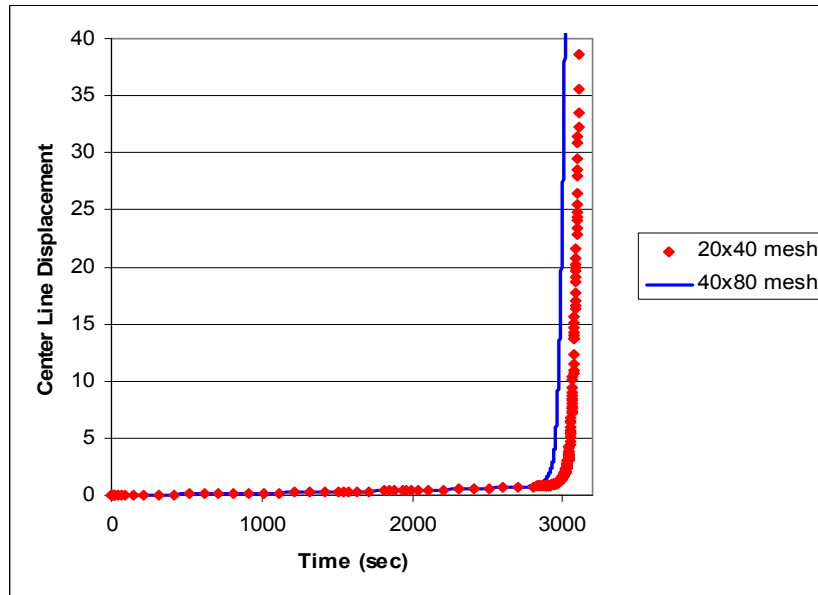


Figure 39.—Nodal displacement at centerline versus time for both meshes.

4. Summary and Conclusions

The finite element method provides a viable approach for assessing the integrity, reliability, and life expectancy of structural components operating under complex thermomechanical/multi-axial loading conditions. The effective use of the finite element technique depends heavily on three main factors: (i) the choice of suitable mathematical models which provide the macroscopic/phenomenological representations of the inelastic constitutive properties and materials damage; (ii) the associated algorithmic developments of efficient and robust schemes for their computer implementation; and (iii) the necessary characterization of the new damage material parameters and (iv) the ability to carry out detailed large-scale simulations for pre- and post-failure structural responses. The research work presented in this report covered these three areas in some detail, with particular emphasis on characterization and numerical simulations of material damage modeling.

The extensions to the GVIPS model to include damage have been completed. The GVIPS model now includes the capability to model both strength and stiffness damage mechanisms. The associated modifications to the fully implicit integration algorithm have also been completed. This includes the implementation of the GVIPS model in both the COMPARE software and the standalone ABAQUS UMATS. As will be described below, extensive numerical testing through numerical simulations were completed. In addition, the newly formulated sensitivities for the damage material parameters were verified by comparing them to finite difference calculations.

The previously developed software COMPARE graphical user interface was extended to include the necessary damage characterization capabilities for both the stiffness and strength reduction mechanisms of damage. Subsequently, these newly implemented features in COMPARE were utilized to perform an initial characterization of the material system TIMETAL21S in the context of tertiary creep curves. The results obtained from this characterization demonstrate the utility of the newly developed capabilities of the GVIPS damage formulation and the extended COMPARE software.

The numerical robustness of the GVIPS damage formulation and the associated algorithmic developments of the fully implicit integration scheme utilized in the developed ABAQUS UMATs (as well as COMPARE itself) are demonstrated through a series of strain localization problems. Particular attention was paid to localization simulations involving arbitrary morphologies (i.e., curved band geometries, band-multiplicity, different band width and orientation). The results of these simulations demonstrated the ability of the material model to provide proper finite limiting sizes for the energy dissipation regions and the “objectivity” of the computations with respect to the final overall load – deformation response curves relative to the degree of mesh refinement. In addition, irrespective of the control mode of loading (displacement versus force controls), these examples have clearly demonstrated that unique (objective) results are always obtained, e.g., peak- and residual-forces, or time-to-failure under constant forces, etc.

References

1. A.F. Saleeb, T.E. Wilt, and W. Li, “An Implicit Integration Scheme For Generalized Viscoplasticity with Dynamic Recovery,” *Computational Mechanics*, vol. 21, no. 6, 1999, pp. 429–440.
2. A.F. Saleeb, T.E. Wilt, and W. Li, “Robust Integration Schemes for Generalized Viscoplasticity with Internal-State Variables,” *Computers and Structures*, vol. 74, 2000, pp. 601–628.
3. Saleeb, A.F. and Wilt, T.E., “Analysis of the Anisotropic Viscoplastic-Damage Response of Composite Laminates—Continuum Basis and Computational Algorithms,” *Int. J. Numer. Meth.* vol. 36, pp. 1629–1660, 1993
4. A.F. Saleeb, S.M. Arnold, M.G. Castelli, T.E. Wilt, and W. Graf, “A General Hereditary Multimechanism-Based Deformation Model With Application to The Viscoelastoplastic Response of Titanium Alloys,” *Inter. Journal of Plasticity*, vol. 17, 2001, pp. 1305–1350.
5. R. Hill, *Mathematical Theory of Plasticity*, Oxford, Clarendon Press, 1983.
6. W. Prager and P.G. Hodge, *Theory of Perfectly Plastic Solids*, New York, Wiley, 1961.
7. S. Wiggins, “Introduction to Applied Nonlinear Dynamical Systems and Chaos,” Springer-Verlag, N.Y., 1990.

REPORT DOCUMENTATION PAGE*Form Approved*
OMB No. 0704-0188

Public reporting burden for this collection of information is estimated to average 1 hour per response, including the time for reviewing instructions, searching existing data sources, gathering and maintaining the data needed, and completing and reviewing the collection of information. Send comments regarding this burden estimate or any other aspect of this collection of information, including suggestions for reducing this burden, to Washington Headquarters Services, Directorate for Information Operations and Reports, 1215 Jefferson Davis Highway, Suite 1204, Arlington, VA 22202-4302, and to the Office of Management and Budget, Paperwork Reduction Project (0704-0188), Washington, DC 20503.

1. AGENCY USE ONLY (Leave blank)		2. REPORT DATE September 2005	3. REPORT TYPE AND DATES COVERED Final Contractor Report	
4. TITLE AND SUBTITLE On Extending the Capabilities of COMPARE to Include Material Damage			5. FUNDING NUMBERS WBS-22-251-92-10 NCC3-992	
6. AUTHOR(S) Atef F. Saleeb and Thomas E. Wilt				
7. PERFORMING ORGANIZATION NAME(S) AND ADDRESS(ES) University of Akron 302 Buchtel Mall Akron, Ohio 44325-0002			8. PERFORMING ORGANIZATION REPORT NUMBER E-15172	
9. SPONSORING/MONITORING AGENCY NAME(S) AND ADDRESS(ES) National Aeronautics and Space Administration Washington, DC 20546-0001			10. SPONSORING/MONITORING AGENCY REPORT NUMBER NASA CR-2005-213815	
11. SUPPLEMENTARY NOTES Project Manger, Steven M. Arnold, Structures and Acoustics Division, NASA Glenn Research Center, organization code RSL, 216-433-3334.				
12a. DISTRIBUTION/AVAILABILITY STATEMENT Unclassified - Unlimited Subject Categories: 24 and 39 Available electronically at http://gltrs.grc.nasa.gov This publication is available from the NASA Center for AeroSpace Information, 301-621-0390.			12b. DISTRIBUTION CODE	
13. ABSTRACT (Maximum 200 words) The work reported herein focuses on three main aspects related to the development of general, time-dependent, material models for the fully coupled deformation-damage analysis of structures. On the theoretical side, we maintained the general thermodynamic framework utilized before for the "pure" deformation modeling part; i.e., complete potential (associative) structure for all the evolution laws pertinent to the damage state variables of both stiffness degradation and strength reduction type. For material characterization, from general test matrices (monotonic or cyclic loading under uniaxial or combined biaxial test cases), we have implemented the necessary stress/state updating algorithms and sensitivity arrays into the automated program COMPARE to determine the material parameters in the extended deformation-damage model. Finally, an extensive number of case studies were included to demonstrate the efficiency and robustness of the developed algorithms in large-scale finite-element simulations. In particular, this included various cases leading to the emergence of failure modes together with the associated details of strain localization zones that are typical in analysis of softening behavior due to damages.				
14. SUBJECT TERMS Deformation; Damage; Inelastic; Finite element; Material parameter estimation			15. NUMBER OF PAGES 44	
			16. PRICE CODE	
17. SECURITY CLASSIFICATION OF REPORT Unclassified	18. SECURITY CLASSIFICATION OF THIS PAGE Unclassified	19. SECURITY CLASSIFICATION OF ABSTRACT Unclassified	20. LIMITATION OF ABSTRACT	

